The Analysis and Prediction of Microphysical States and Polarimetric Radar Variables in a Mesoscale Convective System Using Double-Moment Microphysics, Multi-Network Radar Data, and the Ensemble Kalman Filter

Bryan J. Putnam[1, 2, 3], Ming Xue[1, 2], Youngsun Jung[1], Nathan Snook[1], and Guifu Zhang[2, 3]

[1] Center for Analysis and Predication of Storms, Norman, Oklahoma
[2] Advanced Radar Research Center, Norman, Oklahoma
[3] School of Meteorology, University of Oklahoma, Norman, Oklahoma 73072

Submitted to Monthly Weather Review
January 2013
Revised June 2013
Accepted August 2013

Corresponding author address:
Ming Xue
Center for Analysis and Prediction of Storms
University of Oklahoma,
120 David Boren Blvd., Norman, OK 73072
mxue@ou.edu

Abstract

Doppler radar data are assimilated with an ensemble Kalman Filter (EnKF) in combination with a double-moment (DM) microphysics scheme in order to improve the analysis and forecast of microphysical states and precipitation structures within a mesoscale convective system (MCS) that passed over western Oklahoma on 8-9 May 2007. Reflectivity and radial velocity data from 5 operational WSR-88D S-band radars as well as 4 experimental CASA X-band radars are assimilated over a one hour period using either single-moment (SM) or DM microphysics schemes within the forecast ensemble. Three-hour deterministic forecasts are initialized from the final ensemble mean analyses using a SM or DM scheme, respectively. Polarimetric radar variables are simulated from the analyses and compared with polarimetric WSR-88D radar observations for verification. EnKF assimilation of radar data using a multi-moment microphysics scheme for an MCS case has not previously been documented in the literature.

The use of DM microphysics during data assimilation improves simulated polarimetric variables through differentiation of particle size distributions (PSDs) within the stratiform and convective regions. The DM forecast initiated from the DM analysis shows significant qualitative improvement over the assimilation and forecast using SM microphysics in terms of the location and structure of the MCS precipitation. Quantitative precipitation forecasting skills are also improved in the DM forecast. Better handling of the PSDs by the DM scheme is believed to be responsible for the improved prediction of the surface cold pool, a stronger leading convective line, and improved areal extent of stratiform precipitation.

551. Introduction

Successful convective-scale numerical weather prediction (NWP) requires both accurate initial conditions and a prediction model capable of accurately simulating deep, moist convection. One of the more difficult aspects of simulating convection is the parameterization of the microphysical (MP) processes, including accurate representation of the particle size distribution (PSD) of the hydrometeors. MP processes, such as collision and coalescence, drop breakup, freezing/melting, evaporation/sublimation, and precipitation sedimentation, are highly non-linear and can vary substantially over small spatial and temporal scales (Larson et al. 2005; Wang et al. 2012). Non-linearity can greatly increase the sensitivity of the forecast to the initial conditions due to the complex nonlinear interactions, regime changes, and possible bifurcations (Lorenz 1969). Additionally, model error, such as that associated with uncertainty in the model MP parameterization, can quickly become the dominant factor in error growth even for NWP forecasts with relatively accurate initial conditions (Houtekamer et al. 2005).

In reality, hydrometeors compromise a continuous spectrum of varied sizes and frequency of occurrence. Such continuous PSDs are sometimes approximated using a bin model where hydrometeors are distributed explicitly in groups based on diameter or mass (Khain et al. 2004). While preferable, this approach is computationally very expensive and thus not commonly used in NWP models. Instead, MP processes are typically parameterized using a bulk MP (BMP) approach that assumes PSDs with a specified functional form. One such form is the generalized gamma distribution,

$$N(D)_x = N_{0x} D_x^{\alpha} e^{-\lambda D} \ , \qquad (1)$$

where *N(D)* is the number of hydrometeors of a particular species (denoted by subscript *x*) of a certain diameter in a given volume, and *D* (mm) is the hydrometeor diameter (Ulbrich 1983). Three independent parameters control the shape of the distribution: the intercept N_0 (mm^{-1}m^{-3}), shape α, and slope Λ (mm^{-1}) parameters. Currently, most NWP models use a single-moment (SM) MP scheme where N_0 and α are given fixed values (α is often set to zero) while mass content, which is proportional to the third moment of the PSD, is predicted in the model, allowing Λ to vary independently during the forecast. As available computational resources increase, MP schemes that predict more than one moment have become practical; such schemes are referred to as multi-moment (MM) MP schemes. Double-moment (DM) schemes typically predict mass content and total number concentration (zeroth moment) so that Λ and N_0 can effectively vary independently (α can be either set to a fixed value or diagnosed), while triple-moment (TM) MP schemes predicts three PSD moments, allowing all three parameters to vary independently.

Several recent studies have shown that MM schemes produce more realistic convective storm structure and evolution. Specifically, using a DM scheme instead of a SM scheme has been shown to significantly improve the representation of thermodynamic and MP processes in supercells. For example, Dawson et al. (2010) found that a DM scheme better represents the amount of evaporation in the rear flank downdraft of a supercell because the variable intercept parameter allows the smallest drops in the PSD to be removed first. This results in more realistic cold pool size and intensity due to reduced evaporation cooling. More recently, Jung et al. (2012, hereafter JXT12) demonstrated that a DM MP scheme used within an ensemble Kalman filter (EnKF) data assimilation (DA) system produces more realistic polarimeteric signatures in supercell storms compared to a SM scheme, because the DM scheme allows for size sorting of precipitating particles. For instance, the Z_{DR} arc signature commonly seen at the southern edge of forward flank radar echo is evident when using a DM scheme, but absent when using a SM scheme. Both of these prior studies focused on a supercell storm.

Weather radar currently provides the most complete temporal and spatial sampling of hydrometeors over the entire volume of a storm. Advanced DA methods seek to optimally combine such observations with the background model state to best represent the current state of the atmosphere (Kalnay 2002). The EnKF (Evensen 1994; Evensen 2003) method has been successfully used to assimilate radar observations in various convective-scale observed system simulation experiments (OSSEs) (Snyder and Zhang 2003; Zhang et al. 2004; Tong and Xue 2005; Xue et al. 2006) as well as in experiments using real data (Dowell et al. 2004; Lei et al. 2009; Dowell et al. 2011; Snook et al. 2011, hereafter SXJ11; JXT12). Tong and Xue (2005) and Dowell et al. (2011) used a SM ice MP scheme; JXT12 included a DM scheme but only during assimilation.

EnKF has advantages when coupled with a MM MP scheme. While the four-dimensional variational (4DVAR) method has been shown to work very well for large-scale NWP, its application at the convective scale has been limited to experiments using warm-rain MP or very simple ice MP schemes; thus far it has not been successfully coupled with either a SM or MM MP scheme containing complex ice processes. The EnKF appears to be much better suited for handling the complex nonlinear ice processes required for accurate convective-scale NWP. Xue et al. (2010) showed for the first time that MP state variables, including the hydrometeor mixing ratios and total number concentrations, associated with a DM scheme using 4 ice categories could be estimated accurately from simulated radar data for a supercell. JXT12 further obtained realistic analyses of MP state and polarimetic radar variables within a supercell using real data from a WSR-88D radar and EnKF coupled with a DM scheme. Neither Xue et al. (2010) nor JXT12 examined subsequent forecasts starting from the estimated states.

In this study, observations from multiple radar networks of a mesoscale convective system (MCS) that occurred over Oklahoma and Texas on May 8-9, 2007 are assimilated using an EnKF with either a SM or DM MP scheme. Simulated polarimetric variables from the estimated MP states are verified against independent polarimeteric radar observations to assess the ability of EnKF DA to retrieve information on MP processes occurring within the MCS as well as the performance and impacts of the MP schemes. Deterministic forecasts initialized from the final ensemble mean analyses for various experiments are assessed based on the predicted structure of the MCS, including the accuracy of simulated polarimetric fields.

Earlier related studies have focused almost exclusively on supercells; the MCS investigated in this study presents different challenges. Supercells are characterized by strong rotating updrafts and associated forward and rear flank downdrafts. These features lead to documented polarimetric signatures such as the Z_{dr} arc, Z_{dr} and K_{dp} columns, and mid-level Z_{dr} ring (Kumjian and Ryzhkov 2008). On the other hand, the updrafts associated with an MCS are usually not rotational and the convective system is often divided into convective and stratiform precipitation regions (Fritsch and Forbes 2001). The convective updrafts on the leading edge of the system lead to size sorting of drops which is often characterized by an increase in Z_{dr} (Park et al. 2009). Additionally, the PSD characteristics of the leading convective precipitation and trailing stratiform precipitation differ. Zhang et al. (2008) found that convective rainfall generally has a broad PSD while stratiform rain is dominated by moderately-sized drops. The investigation of an MCS sets this study apart from a very limited number of earlier studies that explore advanced DA, the use of MM MP schemes, and the estimation of multiple MP and polarimetric variables and in particular their combinations. At the completion of our study, JXT12 was the only published real data study assimilating radar data using EnKF with a multi-moment microphysics scheme. A recent paper by Yussouf et al. (2013) addresses similar issues with a different modeling system but both studies deal with supercell storms whose behaviors and dynamics can be quite different from MCSs.

The remainder of this paper is organized as follows: section 2 presents an overview of the May 8-9, 2007 MCS event; section 3 describes the model, radar data, EnKF DA system and experimental setups; section 4 presents the results; and section 5 provides a summary of the significant conclusions.

2. Overview of the May 8-9 2007 MCS

A mesoscale convective system (MCS) and associated line end vortex (LEV) moved through portions of Oklahoma and Texas on 8-9 May 2007. At 1200 UTC on the 8th, a positively tilted upper level trough extended from the Dakotas southwest to New Mexico. An area of low pressure was in place over extreme southwest Texas near the Rio Grande resulting in moist, southeasterly low-level flow from the Gulf over the southern High Plains. Ample moisture, lift aloft, and upslope flow led to the steady development of convection throughout the morning in extreme eastern New Mexico and west Texas (Fig. 1). The outflow from the storms reinforced an already present baroclinic zone, helping to maintain the convection and increase its coverage, thus leading to the development of the MCS. Destabilization from daytime surface heating ahead of the convective line helped to maintain the system as it moved eastward through western Texas [Storm Prediction Center (SPC) 2012b].

The unstable air mass ahead of the MCS resulted in widespread storm development, including some supercells. Schenkman et al. (2011) propose that the ingestion of one of these supercell storms by the MCS led to the development of an LEV on the northern side of the MCS near Wichita Falls, TX around 2200 UTC. Steered by southwesterly upper-level flow during the late afternoon and evening (see Fig. 1), the northern portion of the MCS and its associated LEV moved northeastward into western Oklahoma by 0000 UTC 9 May. The period of particular interest for this case is from 0000 to 0500 UTC as the LEV moved along and just northwest of a Lawton to Oklahoma City line. Throughout this period, the MCS was within the asymmetric stage of MCS development (Fritsch and Forbes 2001) and consisted of an area of leading stratiform precipitation ahead of the LEV, a leading line of intense convection to the east and southeast of the LEV, and a secondary line of trailing stratiform precipitation left over from the portion of the leading convective line that had extended further south into Texas earlier in the afternoon (Fig. 2)

Another supercell was ingested around 0200 UTC that strengthened the vortex in the vicinity of Lawton (Schenkman et al. 2011). Shortly thereafter, four EF-1 tornadoes occurred west of Oklahoma City near the center of the LEV. Additionally, an area of widespread heavy rain (in excess of 50 mm in a three hour period) was observed between Lawton and Oklahoma City, leading to multiple flash flood reports and requiring at least one water rescue [National Weather Service (NWS) 2012]. After 0500, the LEV moved into north central Oklahoma where it gradually dissipated as it entered cooler, more stable air resulting from earlier thunderstorms in Arkansas (SPC 2012a).

3. Data and methods

Two experiments are conducted that include a one-hour assimilation period and three-hour forecasts initialized from the final ensemble mean analyses (EXP_S_M_3_5/EXP_S and EXP_D_M_3_5/EXP_D). These two experiments differ by the MP scheme used during the DA and forecast period. Additional tests were conducted during the assimilation period by varying the covariance inflation options and the assumed observation error in order to determine the optimal DA configurations. All experiments are summarized in Table 1. The experiment names use one letter to identify the type of microphysical scheme used ('S' for the SM MP scheme and 'D' for the DM MP scheme), followed by one letter to indicate the type of spread maintenance used during the data assimilation period ('M' for multiplicative covariance inflation, 'A' for additive perturbation, or 'R' for covariance relaxation) and two numbers to indicate the magnitude of assumed observation errors of radial velocity (V_r) error in m s^{-1} and reflectivity (Z) error in dBZ. Details of the experiments are given in the following section.

a) Model and general experiment setup

The Advanced Regional Prediction System model (ARPS) (Xue et al. 2000; Xue et al. 2001;

Xue et al. 2003) is used as the prediction model in this study. Briefly, ARPS is a fully compressible, non-hydrostatic, three dimensional atmospheric model suitable for NWP from regional to convective scale. ARPS predicts the three wind components (u, v, and w) as well as potential temperature (θ), pressure (p), water vapor mixing ratio (q_v), and several MP state variables that vary depending on the MP option used. For SM MP schemes, only cloud water (q_c), rainwater (q_r), ice (q_i), snow (q_s), graupel (q_g), and/or hail (q_h) mixing ratios are predicted. When a DM MP scheme is used, the total number concentrations of cloud water (N_{tc}), rainwater (N_{tr}), ice (N_{ti}), snow (N_{ts}), graupel (N_{tg}), and hail (N_{th}) are predicted in addition to the mixing ratios.

The model configurations used are largely inherited from SXJ11. The model domain has 259 × 259 × 43 grid points with a horizontal grid spacing of 2 km and stretched vertical grid spacing with a minimum vertical spacing of 100 m at the surface and an average vertical spacing of 500 m. The model top is located 20 km above the surface. The domain covers much of the Texas panhandle, northwest and north central Texas, and western and central Oklahoma (see Fig. 2). Full model physics are used (Xue et al. 2001), including the National Aeronautics and Space Administration (NASA) Goddard Space Flight Center long- and shortwave radiation parameterization, a two-layer soil model, surface fluxes parameterized using predicted surface temperature and water content, and a 1.5-order turbulent kinetic energy (TKE) based subgrid-scale turbulence parameterization, along with high-resolution terrain. As in SXJ11, an initial 1-hour-long deterministic "spin-up" forecast is run from the National Centers for Environmental Prediction (NCEP) North American Mesoscale Model (NAM) analysis at 0000 UTC to 0100 UTC, 9 May 2007. Radar data are then assimilated between 0100 and 0200 UTC at 5 minute intervals. Finally, a 3 hour deterministic forecast is initialized from the final ensemble mean analysis at 0200 UTC. Fig. 3 contains a diagram of the experiment period. For the entire period, lateral boundary conditions are provided by the NCEP NAM 6-hourly analyses and intervening 3-h forecasts. The key difference of this study from that of SXJ11 is the use of different MP schemes, including a DM scheme, within the EnKF DA and the subsequent prediction; details on the EnKF DA will be provided later in section d. Additionally, the inclusion of forecasts expands further on previous work by JXT12 that considered MM MP schemes and the estimation of polarimetric variables for a real supercell case but did not include any forecasts.

b) Radar data

Data are assimilated from 5 WSR-88D S-band radars: KTLX (Oklahoma City/Twin Lakes, OK), KVNX (Vance Air Force Base, OK), KAMA (Amarillo, TX), KLBB (Lubbock, TX), and KDYX (Abilene, TX). Unfortunately, level II data from KFDR (Fredrick, OK) within the region are not available for this case. Data are also assimilated from the 4 radars of the X-band network run by the Engineering Research Center for Collaborative and Adaptive sensing of the Atmosphere (CASA, McLaughlin et al. 2009) network: KCYR (Cyril, OK), KSAO (Chickasha, OK), KLWE (Lawton, OK), and KRSP (Rush Springs, OK), giving a total of 9 radars (Fig. 2). Observations are interpolated horizontally onto the model grid but left at the same vertical location (Xue et al. 2006) and interpolated from the times of scan elevations to the assimilation times (SXJ11). Only Z and V_r observations are used for data assimilation. In addition to those radars used for assimilation, polarimetric observations from the National Severe Storms Laboratory's dual-polarimetric S-band research radar, KOUN (Norman, OK), are used for the independent verification of the simulated polarimetric variables. More detailed information on the radars is summarized in Table 2.

Quality control procedures are included in the ARPS package and are performed on the WSR-88D and KOUN observations before use. These include despeckling and the removal of ground clutter for Z and velocity de-aliasing (unfolding) (Brewster et al. 2005). Additionally, for the KOUN polarimetric data used for verification, differential reflectivity (Z_{DR}) and specific differential phase (K_{DP}) values are not considered when cross-correlation coefficient (ρ_{hv}) is less than 0.8 since the model results do not simulate effects from non-meteorological scatterers. These data are interpolated to the time of verification at each elevation from the previous and following volumes. CASA data are subject to quality control during signal processing, including the removal of ground clutter and velocity de-aliasing as well as range overlay suppression (removal of range-ambiguous data) (Bharadwaj et al. 2010). Attenuation correction is also performed on the CASA radar data.

c) Base experiments using single- and double-moment microphysics schemes

As previously introduced, experiments are conducted using SM or DM MP schemes during the assimilation and forecast periods (Table 1). EXP_S_M_3_5 and EXP_D_M_3_5 are two base DA experiments, using SM and DM MP schemes during the assimilation period, respectively.

EXP_S_M_3_5 is the same as CNTL of SXJ11 in which a combination of multiple SM MP schemes is used in the EnKF ensemble to increase ensemble spread. The 40 member ensemble includes 16 Lin et al. (1983) (LIN) members, 16 Weather Research and Forecasting (WRF) SM 6-class MP scheme (WSM6, Hong and Lim 2006) members, and 8 simplified NWP explicit MP (NEM) members (Schultz 1995). Fewer NEM members are included because the scheme was shown to have a higher root mean square innovation (RMSI) during assimilation in comparison to the more complex LIN and WSM6 schemes in Snook et al. (2012). The use of the LIN and WSM6 schemes, which include hail and graupel categories, respectively, helps enhance the physics diversification within the ensemble. The differences between these species including particle density and N_0 are considered in the Z observation operator during assimilation. The LIN scheme, shown to perform the best in Snook et al. (2012), is used for the free forecast starting from the final ensemble mean analysis at 0200 UTC. The values of the fixed intercept parameters used in the SM schemes are the same as in SXJ11: 8×10^5 m^{-4} for rain (N_{0r}), 3×10^6 m^{-4} for snow (N_{0s}), and 4×10^4 m^{-4} for hail (N_{0h}). Additionally, hydrometeor densities are fixed at 917 kg m^{-3} for ice, 100 kg m^{-3} for snow, and 913 kg m^{-3} for hail. The N_{0r} used is reduced by a factor of 10 compared to the default value of the LIN scheme following Snook and Xue (2008), who found that the original value for N_{0r} led to unrealistically intense surface cold pools resulting from excessive evaporative cooling.

The DM scheme used is that of Milbrandt and Yau (2005a, b) (MY). During the EnKF assimilation period, the shape parameters for hail and rain are varied between 0 and 2 among the ensemble members. Among the 40 members, the rain shape parameter is increased from 0.05 to 2.0 in increments of 0.05, while the hail shape parameter is decreased from 1.95 to 0.0 in increments of 0.05. Varying the shape parameter within the EnKF members has been shown to help increase the ensemble spread and improve performance when uncertainties exist with the parameter values (Xue et al. 2010; JXT12). The shape parameter is set to 0 during the free forecast period. In all DM experiments, the graupel hydrometeor category is turned off as in JXT12; it was found in previous idealized supercell simulations that removing graupel did not significantly impact storm evolution using the MY DM scheme.

d) Sensitivity experiments

The EnKF algorithm used is the ensemble square-root filter (EnSRF) originally developed by Whitaker and Hamill (2002). Following SXJ11, the initial 40-member ensemble is created by adding random, smoothed, Gaussian perturbations to the initial spin-up forecast at 0100 UTC. The smoothing method used is that of Tong and Xue (2008b) with a correlation length scale of 8 km in the horizontal and 5 km in the vertical. The perturbations are added over the entire domain to u, v, and w with a standard deviation of 2 m s^{-1}, and to θ with a standard deviation of 2 K. This differs from SXJ11, where these perturbations were confined to the areas of existing precipitation. 555555 Perturbations are also added to the mixing ratios of water vapor and all hydrometeor species with a standard deviation of 0.001 kg kg^{-1} but are confined to grid points within 1 km of observed radar echoes exceeding 5 dBZ. The latter helps prevent introducing spurious precipitation into the initial ensemble.

Level II Z and V_r data are assimilated from all 9 WSR-88D and CASA radars every 5 minutes within the 1 hour assimilation window. The first EnKF analysis occurs at 0105 UTC when the 5 minute ensemble forecasts from the initial perturbed ensemble are used within the EnKF. The covariance localization radius is 6 km for both Z and V_r observations in the horizontal and vertical and the localization is based on the correlation function of Gaspari and Cohn (1999). For the base or control configurations, the observation error standard deviations are assumed to be 3 m s^{-1} for V_r and 5 dBZ for Z, which are larger than the 1 m s^{-1} and 2 dBZ used in SXJ11. The larger values are believed to better reflect the true errors of the observations used, and are also found to produce ensemble spreads that are more consistent with the errors of the analyzed fields, as shown by sensitivity experiments to be discussed later.

Following SXJ11, to maintain ensemble spread, multiplicative covariance inflation (Anderson 2001) with a factor of 1.25 is applied to the prior ensemble of the base experiments wherever Z_{ob} > 20 dBZ (Xue et al. 2006). Tong and Xue (2005) showed that assimilating clear air Z can help suppress spurious convection. Therefore, all values of Z are assimilated for the WSR-88D radars used. For CASA radars, even though attenuation correction was used, only Z values above a threshold of 20 dBZ are assimilated because of our inability to distinguish between areas of clear air return and completely attenuated regions (SXJ11). For all radars, values of V_r are assimilated only in regions where Z_{ob} > 20 dBZ.

Sensitivity experiments were performed to determine the best covariance inflation configurations and the observation error specifications (Table 1). The covariance inflation includes different combinations of multiplicative covariance inflation, additive perturbation, and covariance relaxation (Zhang et al. 2004). These are indicated by characters M, A and R (denoting the three inflation methods) in experiment names, such as EXP_D_M_1_2, EXP_D_MA_2_3 and EXP_D_R_3_5 in Table 1. The multiplicative inflation factor is 1.25 when used, guided by the earlier study of SXJ11. The additive perturbations used were the smoothed, random, Gaussian perturbations created in the same way as the initial random perturbations described at the beginning of this subsection and added to the ensemble analyses during each EnKF cycle. The standard deviations of the perturbations for u and v wind components and potential temperature θ were 0.5 m s^{-1} and 0.5 K, respectively. Other variables were not perturbed. When covariance relaxation (Zhang et al. 2004) was employed in EXP_D_R_3_5, a relaxation factor of 0.5 was used. All sensitivity experiments used a DM MP scheme.

Sensitivity experiments EXP_D_M_1_2 and EXP_D_MA_2_3 assumed 1 and 2 m s^{-1} error for V_r, and 2 and 3 dBZ error for Z, respectively, as indicated by numbers in their names. Additional sensitivity experiments examining other combinations of values were also tried, but are not described here. The purpose of these experiments is to determine the optimal EnKF configuration (i.e. producing innovation-based ensemble spreads that are consistent with the analysis and forecast errors, given the observation error estimates).

The innovation consistency ratio (Dowell et al. 2004) is used to assess the ensemble consistency. The ratio is defined as the ratio between the sum of observation error variance and ensemble forecast variance in the observation space, to the root-mean-square innovation (RMSI) of the ensemble mean forecast. For a well behaved ensemble system, this ratio should be close to 1 (e.g., Dee 1995).

Fig. 4 shows the consistency ratios for the forecasts during the assimilation period for the sensitivity experiments as well as base experiment EXP_D_M_3_5 when calculated against KTLX and KVNX data; these two radars are chosen because they cover a majority of the storm system. EXP_D_M_1_2, which uses the lowest observation error values, is severely under-dispersive through most of the assimilation period. The additional additive inflation in EXP_D_MA_2_3 together with somewhat larger observation errors, and the use of the relaxation method with a factor of 0.5 combined with the larger observation errors in EXP_D_R_3_5 lead to significant (values over 2) over-dispersion at times in terms of Z and/or V_r. Qualitative analyses of their results showed no overall improvement in comparison to the configurations of experiment EXP_D_M_3_5; therefore, the settings of EXP_D_M_3_5 are used in the base experiments. For the remainder of this paper we will focus on the results of the base experiments EXP_S_M_3_5 and EXP_D_M_3_5 and their respective forecasts. The symbols in the experiment names indicating the inflation methods and observation error magnitudes will be omitted for convenience and the experiments will simply be referred to as EXP_S and EXP_D (Table 1).

4. Results of control experiments

In this section, the results from the base DA experiments, EXP_S and EXP_D, as well as the deterministic forecasts initialized from the corresponding ensemble-mean analyses (Table 1) are discussed. The results of the DA and the final analyses will be examined first, followed by the forecast results.

a) Results of EnKF analyses

Fig. 5 shows a radar mosaic of Z observations from WSR-88D radars KAMA, KDYX, KFWS, KLBB, KTLX, and KVNX at 0200 UTC (Fig. 5a), as well as the 0200 UTC ensemble mean analyses of Z from EXP_S and EXP_D (Fig. 5b, c) at approximately 2 km above ground level (AGL). Both analyses have a reasonably good fit to observed Z and capture the three main features of the system: the leading convective line, the leading stratiform region, and the trailing straitiform region (as defined in Fig. 2). The precipitation structure and intensity in both analyses is generally similar; Z values fall within 10 dBZ of the observations throughout the MCS. More specifically, the analyzed Z is weaker (stronger) in EXP_S (EXP_D) than in the observations in the stratiform regions. Analyzed Z was also noted to be slightly overestimated in some cases when using the MY

DM scheme in JXT12. On the other hand, EXP_D shows some improvement, including better retrieval of the intensity of the leading convective line, especially the southern end, as well as its east/west extent. Some spurious convection develops in the southeast corner of the domain, it should not affect the main MCS much, however.

The performance of the EnKF experiments is evaluated by examining the ensemble spread and the fit of the ensemble mean analyses to the observations in terms of the root mean square innovations (RMSIs). Fig. 6 shows the RMSIs and ensemble spread for Z and V_r for EXP_S and EXP_D; the RMSIs are calculated against KTLX, KVNX, and KDYX radars which have the best coverage of the MCS late in the assimilation period. EXP_D has slightly lower RMSIs for KTLX and KVNX compared to EXP_S, while the forecast error growth (in terms of RMSI) is faster in EXP_S than in EXP_D for all three radars. Error growth is faster for both experiments for KDYX; this is not surprising considering that KDYX mostly covers the trailing stratiform region, which appears to be the most poorly analyzed area in both experiments (see Fig. 5). The prior spread in EXP_S forecasts is higher and more consistent with the RMSI values due to the use of multiple MP schemes within the ensemble. However, the spread in EXP_D is still significant despite the use of a single MP scheme; this may be because of the higher number of degrees of freedom (more variables) involved in a DM scheme and the use of varying shape parameters within the DM scheme of different members. Such differences between SM and DM schemes are similar to those found in JXT12 for a supercell case. The V_r RMSIs are consistently larger than the ensemble spread but both statistics are very similar between the two experiments for all three radars. The difference in MP scheme does not appear to have any significant implication on the filter's handling of the wind fields. Such under-dispersion has been noted in real data cases without leading to filter divergence (Dowell and Wicker 2009; Aksoy et al. 2009; JXT12).

Verification of the model MP state against observations poses additional challenges. Z

measurements alone do not provide adequate information on the true MP state of the atmosphere; the same observed value of Z can correspond to many different hydrometeor PSDs. For example, within a given radar volume, the same value of Z can result from a large number of moderately-sized raindrops or a smaller number of larger raindrops. Additionally, Z alone does not give a full indication as to the types of hydrometeors present. For instance, while the presence of hail can often be inferred due to its intense Z values (values greater than 50 dBZ), the proportions of rain and hail in a rain/hail mixture cannot be directly inferred from observations of Z. For the above reasons, comparing the analyzed Z fields from the two experiments in Fig. 5 is not sufficient to judge the quality of the MP state estimation. Quantities that offer independent information from the directly assimilated variables will be needed to provide more reliable information on the estimated states.

For the MP state variables, polarimetric radar variables can provide valuable independent information. Jung et al. (2008; 2010) developed a polarimetric radar simulator that can be used as the observation operators in DA and for model verifications. The simulator estimates Z at horizontal and vertical polarizations (Z_h, Z_v), differential reflectivity (Z_{DR}), specific differential phase (K_{DP}), and the polarimetric cross-correlation coefficient (ρ_{hv}) from the MP state variables in the model. When combined with polarimetric measurements, this simulator enables indirect verification of the model MP state. For example, Z_{DR} is proportional to the median diameter of PSDs and, therefore, can be used to evaluate the estimates of model PSDs. In this paper, we employ the above polarmetric radar simulator to help evaluate the model analyses and forecasts.

Fig. 7 shows the Z, Z_{DR}, K_{DP} and V_r observations from the 0.5° tilt of KOUN together with the corresponding simulated variables from the 0200 UTC ensemble mean analyses from EXP_S and EXP_D. This lowest tilt of the radar is chosen for evaluation because the polarimetric signatures sought, such as Z_{DR} patterns associated with particle size sorting, are most evident near the surface. Additionally, the current version of the polarimetric simulator used is less robust for ice species with the use of the Rayleigh approximation, so only the rain species is considered. As in the mosaics, the location and intensity of Z in the leading convective line compares reasonably well with observations in both experiments. However, the presence of relatively large raindrops in the leading convective line, implied by high $Z_{DR,}$ is better simulated in EXP_D than in EXP_S. In EXP_S, the Z_{DR} values are too high everywhere mainly because of the reduced N_{0r} value used (Fig. 7f); therefore, the leading convective line is less distinguished from the stratiform regions by containing comparatively large drops. As noted in JXT12, when a SM MP scheme is used, Z and Z_{DR} are monotonically related to q_r and the mean size of the rain DSDs so that a decrease in simulated Z is always accompanied by a decrease in simulated Z_{DR}. Thus, in EXP_S there is a general one-to-one correspondence between Z and Z_{DR} for pure rain so that Z_{DR} is not truly independent of Z. In contrast, high Z_{DR} cores are found to be confined in the convective line in EXP_D, although their values are somewhat over-estimated (Fig. 7j). Excessive size sorting associated with the fixed shape parameter within a two-moment scheme (Milbrandt and Yau 2005a) is thought to be responsible for the overly high Z_{DR} values. The low Z_{DR} observations in this case and in previous studies suggest that stratiform precipitation contains at most moderately sized drops while high Z_{DR} observations indicate the leading convective line contains the largest drops in the system (Zhang et al. 2008). Thus, it is expected that the Z_{DR} values in the leading convective line should be noticeably higher compared to the stratiform region due to the overall larger drop sizes there.

The q_r and N_{0r} fields, displayed in Fig. 8, further demonstrate how the DM scheme used in EXP_D represents the DSDs in different regions. For N_{0r}, a scale of $10\log_{10}$ is used to reduce the dynamic range. Contours of Z are overlaid on $10\log_{10}(N_{0r})$ at 20 dBZ intervals to identify changes in precipitation intensity. The constant N_{0r} of the SM scheme used in EXP_S corresponds to 59 on the $10\log_{10}$ scale. The results are plotted at the surface where the difference between two analyses is greatest due to the differences in the sedimentation and size sorting processes in the schemes. There are several q_r maxima in Fig. 8a that match well with regions of high Z (> 40 dBZ), as indicated by the letters A, B, and C in Fig. 8b. Despite the higher q_r in the leading convective line, the N_{0r} values are lower in this area compared to those in the leading stratiform region, suggesting larger rain drops in the former than in the latter. The N_{0r} values in both the leading and trailing stratiform precipitation regions in EXP_D are similar to the fixed value of EXP_S, but are lower in regions of convective precipitation. Variation of N_{0r} in EXP_D allows for the growth of large drops in more intense convective precipitation as smaller drops are removed, replicating the process of collision-coalescence droplet growth. Similarly, the DM scheme allows for an increase in the number of smaller drops in the stratiform region without an increase in larger drops; this would not be possible using a fixed intercept parameter.

Fig. 7 also contains K_{DP}. The locations of the greatest K_{DP} values are similar to the observations in both EXP_S and EXP_D, being in the vicinity of the heavier precipitation in the leading convective line where the liquid water content is highest. The values in EXP_D are slightly higher than in EXP_S, which follows the proceeding discussion of the PSDs; the lower N_{0r} given the same q_r indicates a greater number of larger drops within the PSD regime to which K_{DP} is more sensitive. K_{DP} values are lower than the observations in both cases, however, which indicates that the amount of rain precipitation is underestimated in both analyses. Though the amount and intensity of precipitation appears similar between the model and observations due to similar Z values, hail is overestimated during the forecast and thus a portion of the total precipitation in both model results contains a hail contribution. Z is sensitive to both rain and hail and different combinations may produce similar Z values, as in this case between the model and observation results, but K_{DP} is not sensitive to hail and thus demonstrates the difference in contribution from both species to the model results and the observations. JXT12 noted a similar high bias in hail with the MY DM scheme. The hydrometeor categories present in the observations were investigated using the fuzzy logic hydrometeor classification scheme of Park et al. (2009) (not shown). The results indicated that there was little hail observed.

The V_r values for both experiments are similar and differ from the observations in the same areas. Both fail to fully resolve the coupling of inbound and outbound velocities that define the circulation at the center of the vortex (indicated by the circle in Fig. 7d) and also contain a notably stronger area of outflow winds along the eastern edge of the northern portion of the leading convective line (indicated by arrows in Fig. 7h and 7l). The outflow in the observations along the leading convective line south of the vortex center is more consistent while both experiments contain a series of bands of outflow winds westward of the noted initial strong outflow along the eastern edge. Nevertheless, the overall wind field is captured relatively well by the filter.

Since KOUN is not used during the assimilation period, its observations provide independent information for observation-space diagnostics of Z, V_r, and the polarimetric variables used for qualitative microphysics verification above. Table 3 contains the correlation coefficients for Z, Z_{DR}, K_{DP}, and V_r calculated against KOUN at the time of the final ensemble mean analysis (0200 UTC). Values for Z and Z_{DR} are higher for EXP_D, consistent with the improvement noted in the qualitative analysis above. Correlation coefficient values for K_{DP} are somewhat higher in EXP_S but are more similar between the two experiments compared to Z_{DR}, where EXP_D shows notable improvement. Correlation coefficient values for V_r are similarly high in the two experiments, as expected from the qualitative similarity in Fig. 7d, 7h, and 7l.

b) Results of forecasts

As described in section 3c, two 3-hour-long deterministic forecasts are made from the 0200 UTC final ensemble mean analyses of EXP_S and EXP_D: a forecast starting from the final analysis of EXP_S using the LIN SM MP scheme and a forecast from the final analysis of EXP_D using the same MY DM MP scheme as during assimilation.

1) Verification of reflectivity forecasts

The convective system initially loses its linear characteristics and becomes predominantly cellular in the EXP_S forecast. Fig. 9 shows the observed WSR-88D radar *Z* mosaic and the forecast results of EXP_S and EXP_D valid at 0230 UTC (30 minute forecast) and 0400 UTC (2 hour forecast). At 0230 UTC, there are many smaller, more isolated convective cores in EXP_S instead of more continuous regions of stratiform precipitation around the LEV and in the trailing line. This also occurs with the convection in the leading convective line. Such a behavior persists through the first hour before a more organized system redevelops. A similar disorganization in the initial forecast was noted in Hu et al. (2006), where it was suggested to be a result of the model microphysics adjusting to the model dynamics. Additionally, Luo et al. (2010) found that the strength of convective updrafts were overestimated in model simulations when using a SM MP scheme. In comparison, the EXP_D forecast maintains a better resemblance to the observations throughout the first hour of the forecast, specifically in the leading stratiform region. The areal coverage of moderate stratiform precipitation on the western and northeastern sides of the leading stratiform region is larger compared to the SM forecasts. Both forecasts handle the trailing stratiform region poorly despite capturing the coverage and intensity of the precipitation relatively well at the end of the assimilation period (0200 UTC).

The MCS is well-developed by the second hour of the forecast in both experiments (Fig. 9d, f). The two-hour forecast of *Z* in EXP_D shows an improvement over EXP_S in terms of the precipitation coverage in the leading stratiform region. While the general location of the convective system is a good match with observations in these cases, the precipitation coverage is considerably under-predicted by EXP_S on both the east and west sides of the LEV. There is also notable spurious precipitation on the west side of the LEV. Under-prediction of the geographic extent of the stratiform regions in EXP_S can be largely attributed to the breakdown of convection organization in the early forecast period (Fig. 9c). This includes isolated regions of intense *Z* that represent convective cores rather than stratiform precipitation in the trailing stratiform region. Although the precipitation intensity is over-predicted in EXP_D, the system is well organized along the entire extent of the line including the consistent and smooth comma-head shaped shield of stratiform precipitation on the north side of the system and a lack of spurious convective precipitation in the trailing stratiform region. Neither of the two cases forecasted the development of new convection southeast and southwest of the main line; this convection may have been better captured if it occurred during the radar data assimilation period, or with a more accurate analysis and prediction of the mesoscale environment, which depends more on non-radar observations.

EXP_D also has an improved leading convective line in comparison to EXP_S. EXP_S has limited leading precipitation that is further west and less intense than observed; it is in the same location as and difficult to differentiate from the trailing stratiform region. Although all forecasts overestimate the intensity of the precipitation on the east side of the LEV, it is most significant in EXP_S with some values over 65 dBZ (Fig. 9d), continuing the trend seen in the early period of the forecast. In EXP_D, Fig. 9f, the location of the northern half of the line matches the observations very well while the southern half arcs more southward compared to observations. Additionally, the distinction between the leading convective line and the beginning of the trailing stratiform region observed is captured better in EXP_D (noted by the arrow in Fig. 9f). There is also a small transition zone (Biggerstaff and Houze 1991) of light (less than 35 dBZ) precipitation between the intense convective precipitation and more moderate stratiform precipitation behind the northern extent of the line.

To see how well the model is predicting the distribution and intensity of precipitation within the convective system, histograms of the *Z* values from every model grid point over the full experiment domain are constructed for the observed Z mosaic and for each forecast (Fig. 10); the mosaic is on the same model grid. The data plotted are separated into 1 dBZ bins for values greater than 15 dBZ.

Both experiments contain values that extend higher in intensity than the observations. However, there is a notable difference in the frequency of values in the 30 to 35 dBZ range; EXP_S has a higher occurrence of that range than either EXP_D or the observations. For EXP_S, an analysis of the vertical distribution Z revealed that the noted convective cores throughout the stratiform regions increased the amount of moderate precipitation falling (not shown). In contrast, EXP_D has higher frequencies for values in the 15 to 25 dBZ range and relatively lower frequencies for values between 30 and 35 dBZ, giving an overall distribution that is closer to that of the observations. The increase in weak Z values in EXP_D is due to the increased coverage of lighter stratiform precipitation on the east and west sides of the LEV. On the other hand, EXP_S consistently overestimates (underestimate) Z greater (lower) than about 30 dBZ. It should be noted that overestimation of these values in EXP_S was not as significant in this case as in SXJ11. The introduction of mesoscale perturbations in the ensemble creation is the sole difference between EXP_S and the control experiment of SXJ11, and appears to have been beneficial. The significantly lower frequency of the low Z values in all three cases is likely connected to both overestimation of intensity of the observed light precipitation and underestimation of the geographical extent of the trailing stratiform precipitation; the absence of newly developed weaker precipitation in the domain should have also contributed.

The improved maintenance of the stratiform region in EXP_D (Fig. 9f) is similar to the findings of Luo et al. (2010) and Morrison et al. (2009), where the development of trailing stratiform precipitation in quasi-linear MCSs was studied using DM MP schemes. Luo et al. (2010) found that the improved development of stratiform precipitation was related to the increase in the detrainment of ice hydrometeors from the convective towers. Fig. 11 shows vertical cross sections of q_s and q_i through the leading convective line and trailing stratiform precipitation of EXP_S and EXP_D, with the cross section locations indicated in Fig. 9d for EXP_S and Fig. 9f for EXP_D. The vertical distributions of q_s and q_i show that there is a dramatic increase in the transport of frozen precipitation over the stratiform region from the leading convective towers in EXP_D compared to EXP_S.

The distributions of the surface q_r, θ, and wind fields in EXP_S and EXP_D help explain the improved precipitation structure of the convective system when using a DM MP scheme (Fig. 12). High q_r values, indicative of more intense convective precipitation, are distributed around the LEV in EXP_S rather than forming a leading line ahead and to the southeast of the LEV as in EXP_D (Figs. 10a and 10b). Figs. 10c and 10d contain the surface θ and wind fields as well as an overlay of the 0.5 g kg^{-1} q_r contours to identify the location of more intense precipitation. A local temperature minimum can be seen behind (on the west side of) the leading convective line in EXP_D, while in EXP_S the temperatures are higher and less consistent in coverage. The distribution of the temperature minimum in EXP_D matches the typical conceptual model of a convective line in an asymmetric system (Fritsch and Forbes 2001) where the use of the DM scheme allows for the size-sorting of smaller drops on the backside of the convective line. The higher number of small drops leads to increased evaporative cooling forming a stronger cold pool on the northwest side of the line. The outflow from this cool, sinking air is seen in the wind field as it spreads out east and westward resulting in convergence on the eastern side of the line. In turn, the convergence helps maintain more intense precipitation at the leading edge of the system. The convective cores remain sporadically distributed in EXP_S without a focused area for new convective development. Additionally, high q_r convective cores are seen within both the leading and trailing stratiform regions in EXP_S in contrast to the consistently lower values seen in EXP_D that help highlight the distinction in the precipitation development in the leading convective line and the stratiform regions as seen in the Z mosaics.

Surface temperature values are evaluated compared to Oklahoma Mesonet observations in Fig. 13. Two time series plots are created for the period 20 minutes before and after 0400 UTC (time of Fig. 12) to capture the passage of the system. The Washington station (“A” in Fig. 12) is chosen due to its location along the leading line while the Ft. Cobb station (“B” in Fig. 12) is chosen due to its location under the stratiform precipitation on the back side of the system, well within the cold pool. Even though the values are not an exact match, EXP_D follows the trends seen in the Mesonet observations better in both cases. The surface temperature in EXP_D decreases along with the observations as the convective line passes the station while the surface temperature in EXP_S remains relatively unchanged. The lack of cooler air at the surface limits the amount of lift to maintain the leading convective line in EXP_S. Additionally, the temperature within the cold pool at the Ft. Cobb station remains unchanged in both EXP_D and the observations while the temperature rapidly increases in EXP_S. It was noted in Fig. 12b that the surface temperature pattern was less consistent compared to EXP_D and associated with the relatively poor system structure seen in EXP_S.

2) QUANTITATIVE VERIFICATION OF REFLECTIVITY AND POLARIMETRIC VARIABLE FORECASTS

Forecast error statistics, such as the equitable threat score (ETS) and reflectivity correlation coefficient (RCC), are often used to quantitatively assess quantitative precipitation forecast (QPF) performance. The ETS, as applied to *Z*, calculates the number of ‘hits’ and ‘misses’ of model forecast *Z* compared to observed *Z* at each model grid point given a certain *Z* threshold while taking into account incidents of random chance over a given verification domain (Wilks 2006). ETS is given by:

$$ETS = \frac{H - H_R}{H + M + FA - H_R} \quad , \qquad (2a)$$

and

$$H_R = \frac{(H+M)(H+FA)}{T}, \qquad (2b)$$

where H, the number of hits, is the total number of model grid points where both forecast and observed Z are equal to or exceed a threshold Z; M , the number of misses, is the total number of model grid points where forecast Z is less than the threshold when there is observed Z above the threshold; FA, 'false alarms', is the total number of model grid points where the forecast Z is greater than the threshold but there is no observed Z above that threshold; H_R is the number of hits expected due to random chance; and T is the total number of hits, misses, false alarms, and model grid points where the forecast Z and observed Z are both below the threshold (a correct 'no'). The observed Z threshold used in this case is 25 dBZ as was used in SXJ11. The RCC is included in addition to ETS because it is less sensitive to location errors and systematic biases; it takes into account the normalized deviation of a value of a given forecast or observed Z at each grid point compared to the their respective average values over the entire domain rather than strictly a yes or no answer (Aksoy et al. 2010). The RCC is defined as

$$r_c = \frac{\sum_{i=1}^{n_o} \left(Z_f - \langle Z_f \rangle\right)\left(Z_o - \langle Z_o \rangle\right)}{\left(\sum_{i=1}^{n_o} \left(Z_f - \langle Z_f \rangle\right)^2 \sum_{i=1}^{n_o} \left(Z_o - \langle Z_o \rangle\right)^2\right)^{\frac{1}{2}}} \qquad (3)$$

where Z_f is the forecast Z, Z_o is observed Z in the model space, $\langle Z_f \rangle$ and $\langle Z_o \rangle$ are the ensemble averages of all forecast and observed Z in the verification domain, and n_o is the number of observed Z grid points above a certain threshold that are included in the calculation. This calculation is implemented differently than in Aksoy et al. (2010) by using the observed Z in the model space rather than the observation space; the former was also done in Schenkman et al. (2011). The threshold Z for this score is 15 dBZ, lower than that for ETS, since RCC is related to deviations from the mean value compared to the more restrictive ETS. The ETS may be saturated with hits if the threshold is too low so correctly capturing the locations of features of interest like the leading convective line, stratiform regions, etc., defined by higher intensity Z will not be emphasized in the score.

Fig. 14 shows the ETS and RCC scores at forecast hours 1, 2, and 3 for all three experiments over the entire forecast domain as well as for a sub-domain (indicated by the black box in Fig. 9b) covering the LEV and leading convective line. EXP_D outperforms EXP_S in terms of both scores over the full domain, indicating that the precipitation coverage is improved and the general precipitation intensity across the system is closer to observations in EXP_D. The improvement seen in EXP_D is increased for both statistics when the calculation is made over the sub-domain focusing on the LEV and leading convective line; the DM scheme used in EXP_D was shown to improve the development of these features significantly. Specifically, ETS decreases at a much slower rate while RCC remains almost constant throughout the 3-hour forecast, indicating that the faster decrease in the scores with time when calculated over the entire domain is related mostly to the trailing stratiform region; Fig. 9f showed that the forecast Z in this region was both less intense and smaller in geographical extent than in the observations. This region was also the most poorly analyzed based on Fig. 5c which may have led to the poorer forecast. However, the full domain scores still indicate that EXP_D is better than EXP_S overall.

The improvement in EXP_D throughout the forecast period is also seen in terms of the simulated polarimetric variables. Fig. 15 shows the root-mean-square differences (RMSDs) calculated at each hour from 0200 to 0500 UTC between the simulated polarimetric variables of EXP_S and EXP_D forecasts at the same 0.5° tilt that was presented in Fig. 7 and the corresponding observations. The calculations were limited to areas where observed ρ_{hv} was 0.9 or greater to avoid interference from non-meteorological scatterers. EXP_D has lower difference for each variable at every hour except for Z at 0200 UTC. The differences also grow more rapidly over time in EXP_S. The larger differences in EXP_S are because of extreme values of Z_{DR} (over 4.5 dB) and K_{DP} (well over 5 deg km^{-1}) associated with high q_r. The one-to-one relationship between Z and Z_{DR} seen in the EXP_S analysis is again apparent in the EXP_S forecast; significant increases in Z_{DR} accompany areas of higher Z. The difference may also be due to the intense convection around the LEV in EXP_S, as discussed earlier. Though the Z_{DR} values in some areas are higher than observed, the Z_{DR} RMSD values are smaller in EXP_D due to consistently lower Z_{DR} values across the stratiform precipitation north of the LEV because of the aforementioned better representation of the stratiform PSD by the DM scheme. The difference in simulated K_{DP} between the two experiments is not as large as that of Z_{DR}, apparently because the intensity of the leading convective line in EXP_D is also overestimated, although not as much as in EXP_S.

5. Summary and conclusions

In this study, an EnKF DA method is used in combination with an advanced double-moment (DM) microphysics (MP) parameterization scheme to improve the representation of the MP state and short-term forecast of an MCS that occurred over Oklahoma and Texas on 8-9 May 2007. Reflectivity (Z) and radial velocity (V_r) data are assimilated from 5 WSR-88D S-band radars and 4 CASA X-band radars over a one hour period. There are two base experiments that use single-moment (SM) MP schemes (EXP_S) and a DM MP scheme (EXP_D) during the assimilation period followed by three-hour deterministic forecasts initialized from the final ensemble mean analyses using a SM and DM MP scheme, respectively. Simulated polarimetric variables from the analyses and forecasts are compared with polarimetric radar observations from polarimetric WSR-88D radar KOUN for independent verification of the model microphysical states in addition to qualitative and quantitative comparisons of the MCS structure and precipitation fields.

The comparisons of simulated polarimetric variables from the final analyses with observations indicate that the use of a DM scheme within the EnKF DA cycles significantly improves the representations of the PSDs of the convective and stratiform precipitation regions of the MCS. For example, differential reflectivity (Z_{DR}) values, which give an indication of the axis ratio of raindrops, are significantly higher in the stratiform region of EXP_S compared to both EXP_D and the observations even though all have similar Z fields. The rain PSD of this light to moderate precipitation typically contains small to moderate sized drops with low aspect ratios. In contrast to the fixed rain intercept parameter (N_{0r}) used in EXP_S, the varying N_{0r} of EXP_D allows for an increase in the number of small to medium sized drops without also increasing the number of large raindrops in regions of lighter precipitation.

Similarly, for the forecast period, use of the DM scheme initialized with the DM analysis leads to improved results over the SM forecast initialized from the SM analysis. Specifically, the MCS structure is improved in terms of both the coverage of precipitation in the stratiform region as well as the intensity and extent of the leading convective line. The MCS in EXP_S breaks down into multiple intense convective cells early in the forecast period and never fully recovers the structure seen in the observations. Analysis of rain mixing ratio fields shows that the heavy convective precipitation remains concentrated linearly in the leading convective line of EXP_D. The size sorting of smaller drops with the DM scheme increases the amount of evaporative cooling on the backside of the line. The resulting cold pool distribution better matches the conceptual model of an MCS which leads to better maintenance of both the leading convective line and stratiform regions. The forecast location and intensity of the forecast reflectivity fields is also shown to be improved quantitatively in terms of both the equitable threat score (ETS) and reflectivity correlation coefficient (RCC).

The improvements noted above in the treatment of PSDs in different precipitation regions as well as a significantly improved structural forecast confirm and provide new insight into the importance of using advanced MM MP schemes for convective scale DA and short-term forecasts. The polarimetric radar simulator proves to be a valuable tool for assessing the quality of analyzed and forecast microphysical states. However, multiple challenges remain to better represent cloud microphysics in convective-scale forecasts. Simulated K_{DP} values show that hail was overestimated in the model results compared to the observations. The graupel category was not included in these experiments in addition to hail, but the lack of this additional natural state for frozen precipitation may have resulted in too many overly-large hailstones. Such biases within the microphysical schemes suggest areas for future study. Furthermore, size sorting is often overestimated when the shape parameter, α, of the gamma size distribution is fixed at 0, as is done in this study (Kumjian and Ryzhkov 2012). A non-zero value of α with a DM scheme or the use of a triple-moment scheme that effective predicts α, may produce better forecasts and dual-pol signatures.

Finally, with the availability of an ensemble of analyses from the EnKF, ensemble forecasts can be produced, which can also include perturbations to N_0 when using SM MP and to α when using DM MP. The impact of the microphysics scheme on the probabilistic forecasting of polarimetric variables has not be examined in the literature and will be examined in a future study, which can be also be considered an extension to Snook et al. (2012).

Acknowledgement This study was primarily supported by NSF grants AGS-0608168, AGS-0802888 and AGS-1046171. The second author was also supported by NSF grants EEC-0313747, OCI-0905040, AGS-0941491, AGS-0750790, and AGS-1046081. Computations were carried out at the Oklahoma Supercomputing Center for Education and Research (OSCER) and on the Kraken system at the National Institute for Computational Sciences.

References

Aksoy, A., D. C. Dowell, and C. Snyder, 2009: A multi-case comparative assessment of the ensemble Kalman filter for assimilation of radar observations. Part I: Storm-scale analysis. *Mon. Wea. Rev.*, **137,** 1805-1824.

Aksoy, A., D. C. Dowell, and C. Snyder, 2010: A multi-case comparative assessment of the ensemble Kalman filter for assimilation of radar observations. Part II: Short-range ensemble forecasts. *Mon. Wea. Rev.*

Anderson, J. L., 2001: An ensemble adjustment Kalman filter for data assimilation. *Mon. Wea. Rev.*, **129,** 2884-2903.

Bharadwaj, N., V. Chandrasekar, and F. Junyent, 2010: Signal processing system for the CASA integrated project I radars. *J. Atmos. Ocean Tech.*, **27,** 1400-1460.

Biggerstaff, M. I. and R. A. Houze, Jr., 1991: Kinematic and precipitation structure of the 10-11 June 1985 squall line. *Mon. Wea Rev.*, **119,** 3034-3065.

Brewster, K., M. Hu, M. Xue, and J. Gao, 2005: Efficient assimilation of radar data at high resolution for short-range numerical weather prediction. *WWRP Int. Symp. Nowcasting Very Short Range Forecasting*, CDROM 3.06.

Dawson, D. T., II, M. Xue, J. A. Milbrandt, and M. K. Yau, 2010: Comparison of evaporation and cold pool development between single-moment and multi-moment bulk microphysics schemes in idealized simulations of tornadic thunderstorms. *Mon. Wea. Rev.*, **138,** 1152-1171.

Dee, D. P., 1995: On-line estimation of error covariance parameters for atmospheric data assimilation. *Mon. Wea. Rev.*, **123,** 112-81145.

Dowell, D., F. Zhang, L. J. Wicker, C. Snyder, and N. A. Crook, 2004: Wind and temperature retrievals in the 17 May 1981 Arcadia, Oklahoma supercell: Ensemble Kalman filter experiments. *Mon. Wea. Rev.*, **132,** 1982-2005.

Dowell, D. C. and L. J. Wicker, 2009: Additive noise for storm-scale ensemble data assimilation. *J. Atmos. Oceanic Technol.*, **26,** 911-927.

Dowell, D. C., L. J. Wicker, and C. Snyder, 2011: Ensemble Kalman filter assimilation of radar observations of the 8 May 2003 Oklahoma City supercell: Influence of reflectivity observations on storm-scale analysis. *Mon. Wea. Rev.*, **139,** 272–294.

Evensen, G., 1994: Sequential data assimilation with a nonlinear quasi-geostrophic model using Monte Carlo methods to forecast error statistics. *J. Geophys. Res.*, **99,** 10143-10162.

Evensen, G., 2003: The ensemble Kalman filter: Theoretical formulation and practical implementation. *Ocean Dynamics*, **53,** 343-367.

Fritsch, J. M. and G. S. Forbes, 2001: Mesoscale convective systems. *Meteor. Monogr.*, **50,** 323-358.

Gaspari, G. and S. E. Cohn, 1999: Construction of correlation functions in two and three dimensions. *Quart. J. Roy. Meteor. Soc.*, **125,** 723-757.

Hong, S.-Y. and J.-O. J. Lim, 2006: The WRF single-moment 6-class microphysics scheme (WSM6). *J. Korean Meteor. Soc.*, **42,** 129-151.

Houtekamer, P. L., H. L. Mitchell, G. Pellerin, M. Buehner, M. Charron, L. Spacek, and B. Hansen, 2005: Atmospheric data assimilation with an ensemble Kalman filter: Results with real observations. *Mon. Wea. Rev.*, **133,** 604-620.

Hu, M., M. Xue, J. Gao, and K. Brewster, 2006: 3DVAR and cloud analysis with WSR-88D level-II data for the prediction of Fort Worth tornadic thunderstorms. Part II: Impact of radial velocity analysis via 3DVAR. *Mon. Wea. Rev.*, **134,** 699-721.

Jung, Y., G. Zhang, and M. Xue, 2008: Assimilation of simulated polarimetric radar data for a convective storm using ensemble Kalman filter. Part I: Observation operators for reflectivity and polarimetric variables. *Mon. Wea. Rev.*, **136,** 2228-2245.

Jung, Y., M. Xue, and G. Zhang, 2010: Simulations of polarimetric radar signatures of a supercell storm using a two-moment bulk microphysics scheme. *J. Appl. Meteor. Climatol.*, **49,** 146-163.

Jung, Y., M. Xue, and M. Tong, 2012: Ensemble Kalman filter analyses of the 29-30 May 2004 Oklahoma tornadic thunderstorm using one- and two-moment bulk microphysics schemes, with verification against polarimetric data. *Mon. Wea. Rev.***,** Accepted.

Kalnay, E., 2002: *Atmospheric Modeling, Data Assimilation, and Predictability*. Cambridge University Press, 341 pp.

Khain, A., A. Pokrovsky, M. Pinsky, A. Seifert, and V. Phillips, 2004: Simulation of Effects of Atmospheric Aerosols on Deep Turbulent Convective Clouds Using a Spectral Microphysics Mixed-Phase Cumulus Cloud Model. Part I: Model Description and Possible Applications. *J. Atmos. Sci.*, **61**.

Kumjian, M. R. and A. V. Ryzhkov, 2008: Polarimetric signatures in supercell thunderstorms. *J. Appl. Meteor. Climatol.*, **47,** 1940-1961.

Kumjian, M. R. and A. V. Ryzhkov, 2012: The Impact of Size Sorting on the Polarimetric Radar Variables. *J. Atmos. Sci.*, **69,** 2042–2060.

Larson, V. E., J.-C. Golaz, H. Jiang, and W. R. Cotton, 2005: Supplying local microphysics parameterizations with information about subgrid variability: Latin hypercube sampling. *J. Atmos. Sci.*, **62,** 4010–4026.

Lei, T., M. Xue, and T. Yu, 2009: Multi-scale analysis and prediction of the 8 May 2003 Oklahoma City tornadic supercell storm assimilating radar and surface network data using EnKF. *Extended abstract, 13th Conf. of IOAS-AOLS, AMS Meetings 2008*, Paper 6.4.

Lin, Y.-L., R. D. Farley, and H. D. Orville, 1983: Bulk parameterization of the snow field in a cloud model. *J. Climat. Appl. Meteor.*, **22,** 1065-1092.

Lorenz, E. N., 1969: Atmospheric predictability as revealed by naturally occurring analogues. *J. Atmos. Sci.*, **26,** 636-646.

Luo, Y., Y. Wang, H. Wang, Y. Zheng, and H. Morrison, 2010: Modeling convective-stratiform precipitation processes on a Mei-Yu front with the Weather Research and Forecasting model: Comparison with observations and sensitivity to cloud microphysics parameterizations. *J. Geophys. Res.*, **115,** D18117.

McLaughlin, D., D. Pepyne, V. Chandrasekar, B. Philips, J. Kurose, M. Zink, K. Droegemeier, S. Cruz-Pol, F. Junyent, J. Brotzge, D. Westbrook, N. Bharadwaj, Y. Wang, E. Lyons, K. Hondl, Y. Liu, E. Knapp, M. Xue, A. Hopf, K. Kloesel, A. DeFonzo, P. Kollias, K. Brewster, R. Contreras, B. Dolan, T. Djaferis, E. Insanic, S. Frasier, and F. Carr, 2009: Short-wavelength technology and the potential for distributed networks of small radar systems. *Bull. Amer. Meteor. Soc.*, **90,** 1797-1817.

Milbrandt, J. A. and M. K. Yau, 2005a: A multi-moment bulk microphysics parameterization. Part I: Aanlysis of the role of the spectral shape parameter. *J. Atmos. Sci.*, **62,** 3051-3064.

Milbrandt, J. A. and M. K. Yau, 2005b: A multi-moment bulk microphysics parameterization. Part II: A proposed three-moment closure and scheme description. *J. Atmos. Sci.*, **62,** 3065-3081.

Morrison, H., G. Thompson, and V. Tatarskii, 2009: Impact of cloud microphysics on the development of trailing stratiform precipitation in a simulated squall line: Comparison of one- and two-moment schemes. *Mon. Wea. Rev.*, **137,** 991-1007.

NWS, cited 2012: Storm Data and Unusual Weather Phenomena - May 2007. [Available online from http://www.srh.noaa.gov/media/oun/stormdata/oun200705.pdf.]

Park, H., A. V. Ryzhkov, D. S. Zrnic, and K.-E. Kim, 2009: The hydrometeor classification algorithm for the polarimetric WSR-88D: description and application to an MCS. *Wea. Forecasting* **24,** 730-748.

Schenkman, A., M. Xue, A. Shapiro, K. Brewster, and J. Gao, 2011: The analysis and prediction of the 8-9 May 2007 Oklahoma tornadic mesoscale convective system by assimilating WSR-88D and CASA radar data using 3DVAR. *Mon. Wea. Rev.*, **139,** 224-246.

Schultz, P., 1995: An explicit cloud physics parameterization for operational numerical weather prediction. *Mon. Wea. Rev.*, **123,** 3331-3343.

Snook, N. and M. Xue, 2008: Effects of microphysical drop size distribution on tornadogenesis in supercell thunderstorms. *Geophy. Res. Letters*, **35,** L24803, doi:10.1029/2008GL035866.

Snook, N., M. Xue, and J. Jung, 2011: Analysis of a tornadic meoscale convective vortex based on ensemble Kalman filter assimilation of CASA X-band and WSR-88D radar data. *Mon. Wea. Rev.*, **139,** 3446-3468.

Snook, N., M. Xue, and Y. Jung, 2012: Ensemble probabilistic forecasts of a tornadic mesoscale convective system from ensemble Kalman filter analyses using WSR-88D and CASA radar data. *Mon. Wea. Rev.*, 2126–2146.

Snyder, C. and F. Zhang, 2003: Assimilation of simulated Doppler radar observations with an ensemble Kalman filter. *Mon. Wea. Rev.*, **131,** 1663-1677.

SPC, cited 2012: May 9, 2007 0100 UTC Day 1 Convective Outlook. [Available online from http://spc.noaa.gov/products/outlook/archive/2007/day1otlk_20070509_0100.html.]

SPC, cited 2012: May 8, 2007 1630 UTC Day 1 Convective Outlook. [Available online from http://spc.noaa.gov/products/outlook/archive/2007/day1otlk_20070508_1630.html.]

Tong, M. and M. Xue, 2005: Ensemble Kalman filter assimilation of Doppler radar data with a compressible nonhydrostatic model: OSS Experiments. *Mon. Wea. Rev.*, **133,** 1789-1807.

Tong, M. and M. Xue, 2008: Simultaneous estimation of microphysical parameters and atmospheric state with radar data and ensemble square-root Kalman filter. Part II: Parameter estimation experiments. *Mon. Wea. Rev.*, **136,** 1649–1668.

Ulbrich, C. W., 1983: Natural variations in the analytical form of the raindrop size distributions. *J. Appl. Meteor.*, **22,** 1764-1775.

Wang, H., T. Auligne, and H. Morrison, 2012: Impact of Microphysics Scheme Complexity on the Propagation of Initial Perturbations. *Mon. Wea. Rev.*, **140,** 2287-2296.

Whitaker, J. S. and T. M. Hamill, 2002: Ensemble data assimilation without perturbed observations. *Mon. Wea. Rev.*, **130,** 1913-1924.

Wilks, D. S., 2006: *Statistical Methods in the Atmospheric Sciences*. Second ed. Academic Press, Elsevier, Amsterdam.

Xue, M., K. K. Droegemeier, and V. Wong, 2000: The Advanced Regional Prediction System (ARPS) - A multiscale nonhydrostatic atmospheric simulation and prediction tool. Part I: Model dynamics and verification. *Meteor. Atmos. Physics*, **75,** 161-193.

Xue, M., M. Tong, and K. K. Droegemeier, 2006: An OSSE framework based on the ensemble square-root Kalman filter for evaluating impact of data from radar networks on thunderstorm analysis and forecast. *J. Atmos. Ocean Tech.*, **23,** 46–66.

Xue, M., Y. Jung, and G. Zhang, 2010: State estimation of convective storms with a two-moment microphysics scheme and an ensemble Kalman filter: Experiments with simulated radar data *Q. J. Roy. Meteor. Soc*, **136,** 685-700.

Xue, M., D.-H. Wang, J.-D. Gao, K. Brewster, and K. K. Droegemeier, 2003: The Advanced Regional Prediction System (ARPS), storm-scale numerical weather prediction and data assimilation. *Meteor. Atmos. Physics*, **82,** 139-170.

Xue, M., K. K. Droegemeier, V. Wong, A. Shapiro, K. Brewster, F. Carr, D. Weber, Y. Liu, and D. Wang, 2001: The Advanced Regional Prediction System (ARPS) - A multi-scale nonhydrostatic atmospheric simulation and prediction tool. Part II: Model physics and applications. *Meteor. Atmos. Phys.*, **76,** 143-166.

Yussouf, N., E. R. Mansell, L. J. Wicker, D. M. Wheatley, and D. J. Stensrud, 2013: The Ensemble Kalman Filter Analyses and Forecasts of the 8 May 2003 Oklahoma City Tornado Supercell Storm using Single and Double Moment Microphysics Schemes. *Mon. Wea. Rev.***,** In Press.

Zhang, F., C. Snyder, and J. Sun, 2004: Impacts of initial estimate and observations on the convective-scale data assimilation with an ensemble Kalman filter. *Mon. Wea. Rev.*, **132,** 1238-1253.

Zhang, G., M. Xue, and D. Dawson, 2008: Diagnosing the intercept parameter for exponential rain drop size distribution based on video disdrometer observations and tests with squall line simulations. *J. Appl. Meteor. Climatol.*, **47,** 2983-2992.

List of figures

Fig. 1. (a) 300mb wind barbs and geopotential height contours (60 dam interval) from the Plymouth State Weather Center as well as (b) 850mb wind barbs, height contours (60 dam interval), temperature (red dashed lines at 2° C interval), and dewpoint (color fill) analysis from the Storm Prediction Center (SPC) at 1200 UTC 8 May 2007.

Fig. 2. Radar reflectivity (dBZ) observation mosaic from KAMA, KDYX, KFWS, KLBB, KTLX, and KVNX at 0200 UTC approximately 2km AGL covering the full experiment domain. Note the locations of the leading convective line, LEV, leading stratiform region, and trailing stratiform regions. The locations of all radars used in this study are also included.

Fig. 3. Diagram of initial spin-up forecast, the EnKF data assimilation cycles, and subsequent forecast for the experiments.

Fig. 4. Consistency ratios during the assimilation period (0105 UTC – 0200 UTC) of experiments EXP_D_M_3_5, EXP_D_M_1_2, EXP_D_MA_2_3, and EXP_D_R _3_5 for KTLX (a) Z and (b) Vr and KVNX (c) Z and (d) Vr data. The time is in seconds starting at 0000 UTC. The optimal value of 1 is indicated by the black dotted line.

Fig. 5. (a) Reflectivity (dBZ) observation mosaic (a) from KAMA, KDYX, KFWS, KLBB, KTLX, and KVNX approximately 2 km AGL and analyzed reflectivity and horizontal wind vectors (m s^{-1}) at 0200 UTC plotted at grid level 10 (about 2 km AGL) for (b) EXP_S and (c) EXP_D. The horizontal wind vectors are plotted every 15 grid points (30 km).

Fig. 6. Average root-mean-square innovation and ensemble spread during the assimilation period for EXP_S and EXP_D for Z (dBZ) calculated against (a) KTLX, (b) KVNX, and (c) KDYX observations as well as (d-f) radial velocity. Time of assimilation is given in seconds based on the start of the experiment at 0000 UTC (0105 UTC – 0200 UTC).

Fig. 7. (a) Reflectivity (dBZ), (b) differential reflectivity (dB), (c) specific differential phase (deg

km^{-1}) , and (d) radial velocity (ms^{-1}) at a .5° tilt from KOUN as well as the ensemble mean final analysis at 0200 UTC for (e-h) EXP_S and (i-l) EXP_D.

Fig. 8. Surface (a) rain water mixing ratio (g kg^{-1}) and (b) intercept parameter values (m^{-3} mm^{-1}, $10\log_{10}$ scale) from the EXP_D final ensemble mean analysis. Reflectivity contours at 20 dBZ intervals are overlaid on (b). The fixed intercept parameter value in EXP_S corresponds to 59 on the $10\log_{10}$ scale.

Fig. 9. Reflectivity (dBZ) observation mosaic from KAMA, KDYX, KFWS, KLBB, KTLX, and KVNX approximately 2 km AGL at (a) 0230 UTC and (b) 0400 UTC as well as (c) 30 minute and (d) 2 hour forecast reflectivity and horizontal wind field (m s^{-1}) at grid level 10 (about 2 km AGL) for EXP_S and (e, f) EXP_D. The horizontal wind vectors are plotted every 15 grid points (30 km).

Fig. 10. Reflectivity frequency histograms plotted for 1 dBZ bins for (a) the KAMA, KDYX, KFWS, KLBB, KTLX, and KVNX radar reflectivity observation mosaic (one the same model grid) and for 2 hour forecast reflectivity from (b) EXP_S and (c) EXP_D.

Fig. 11. Vertical cross sections of (a) snow mixing ratio (g kg^{-1}) and (b) cloud ice mixing ratio (g kg^{-1}) for EXP_S and (c-d) EXP_D. The locations of the cross sections are noted in Fig. 9d for EXP_S and Fig. 9f for EXP_D and extend from point A (left) to point B (right).

Fig. 12. Two hour forecast surface (a) rain water mixing ratio (g kg^{-1}) and (b) potential temperature (K) and horizontal wind field (ms^{-1}) for EXP_S and (c-d) EXP_D. The 0.5 g kg^{-1} rain water mixing ratio contour is overlaid on the potential temperature plots. Horizontal wind vectors are plotted every 5 grid points (10 km).

Fig. 13. Observed as well as interpolated surface temperature (°F) time series plots from EXP_S and EXP_D (UTC) at the location of Oklahoma Mesonet stations (a) Washington and (B) Ft.

Cobb. The station locations are indicated by an ‘A’ for Washington and ‘B’ for Ft. Cobb in Fig. 11c and d.

Fig. 14. (a) Forecast reflectivity ETS and (b) RCC scores for EXP_S and EXP_D at forecast hours 1, 2, and 3 for the entire experiment domain as well as over the (c-d) sub-domain defined in Fig. 9b.

Fig. 15. The RMSDs between simulated polarimetric variables of EXP_S and EXP_D and KOUN observations at a 0.5° tilt for (a) reflectivity of horizontal polarization (dBZ), (b) differential reflectivity (dB), and (c) specific differential phase (deg km^{-1}) throughout the forecast period.

Table 1: List of experiments. Information on the base experiments (DA Experiments), forecast experiments (Forecast EXP), and sensitivity test configurations (Sensitivity Tests) is included. The table lists the MP scheme used during the assimilation period (DA) and the forecast period (F); whether multiplicative inflation (M), additive perturbation (A), or covariance relaxation (R) is used; and what the observation errors are.

Experiments	**SM versus DM scheme**	**Inflation Method**			**Observation Error**	
		M	**A**	**R**	**V_r error**	**Z error**
EXP_S_M_3_5/EXP_S	SM	1.25	N.A.	N.A.	3	5
EXP_D_M_3_5/EXP_D	DM	1.25	N.A.	N.A.	3	5
EXP_D_M_1_2	DM	1.25	N.A.	N.A.	1	2
EXP_D_MA_2_3	DM	1.25	+/- .5 u,v,θ	N.A.	2	3
EXP_D_R_3_5	DM	N.A.	N.A.	0.5	3	5

Table 2: Summary of the characteristics of radars used for assimilation.

	WSR-88D	CASA
Wavelength (cm)	10.0 (S-band)	3.19 (X-band)
Maximum Range (km)	459	40
Peak Power (kW)	750	25
Pulse Repetition Frequency (KHZ)	.3-1.3	<= 3.33
3 dB Beamwidth (°)	0.95	2
Rotation Rate (° s^{-1})	36	Variable up to 120
Antenna Gain (dB)	45	38
Antenna Diameter (m)	8.5	1.5

Table 3: Correlation coefficient statistics for the ensemble mean final analyses of EXP_S and EXP_D calculated against KOUN observations.

Variable	EXP_S	EXP_D
Z	.5638	.6218
V_r	.8626	.8531
Z_{DR}	.4295	.4853
K_{DP}	.5765	.5378

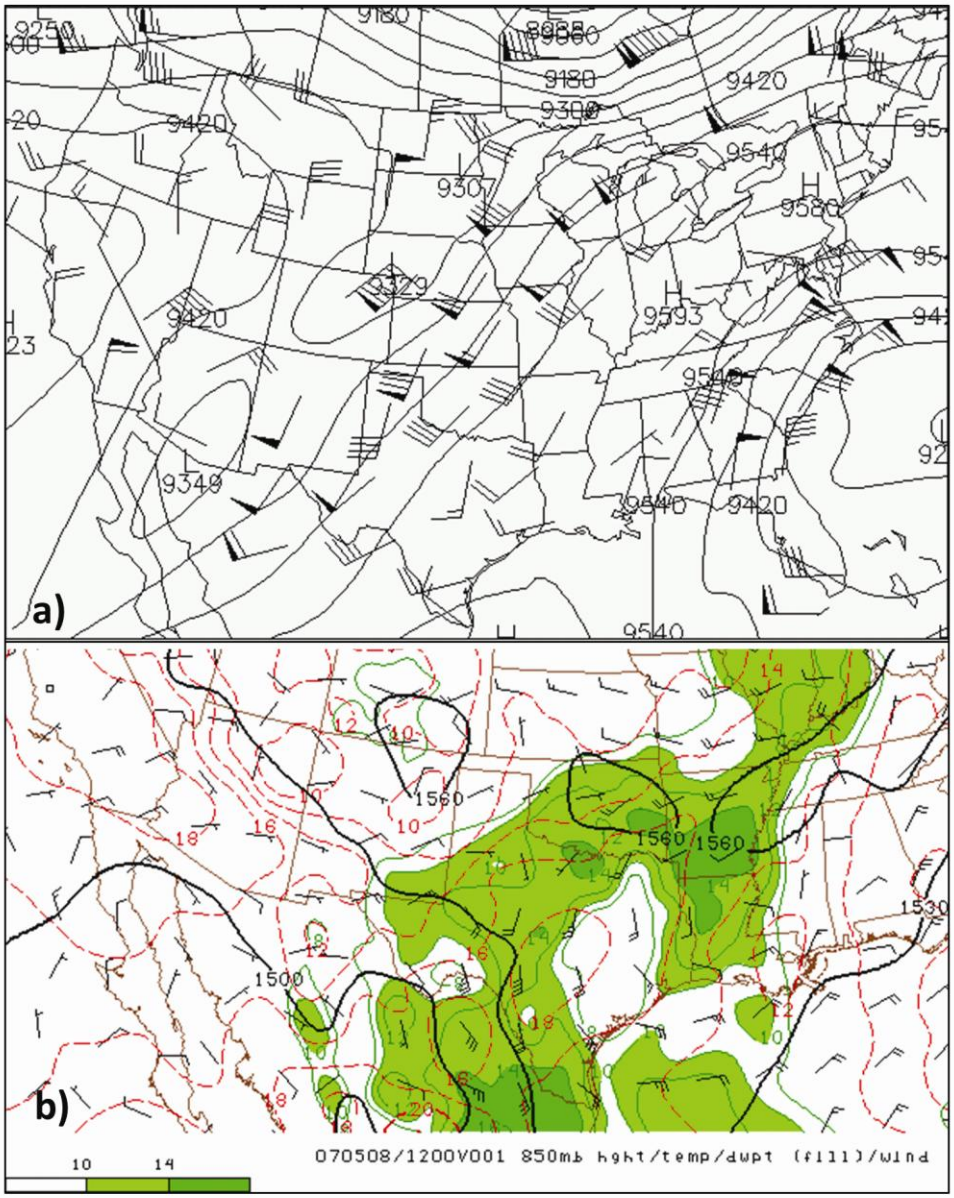

Fig. 1. (a) 300mb wind barbs and geopotential height contours (60 dam interval) from the Plymouth State Weather Center as well as (b) 850mb wind barbs, height contours (60 dam interval), temperature (red dashed lines at 2° C interval), and dewpoint (color fill) analysis from the Storm Prediction Center (SPC) at 1200 UTC 8 May 2007.

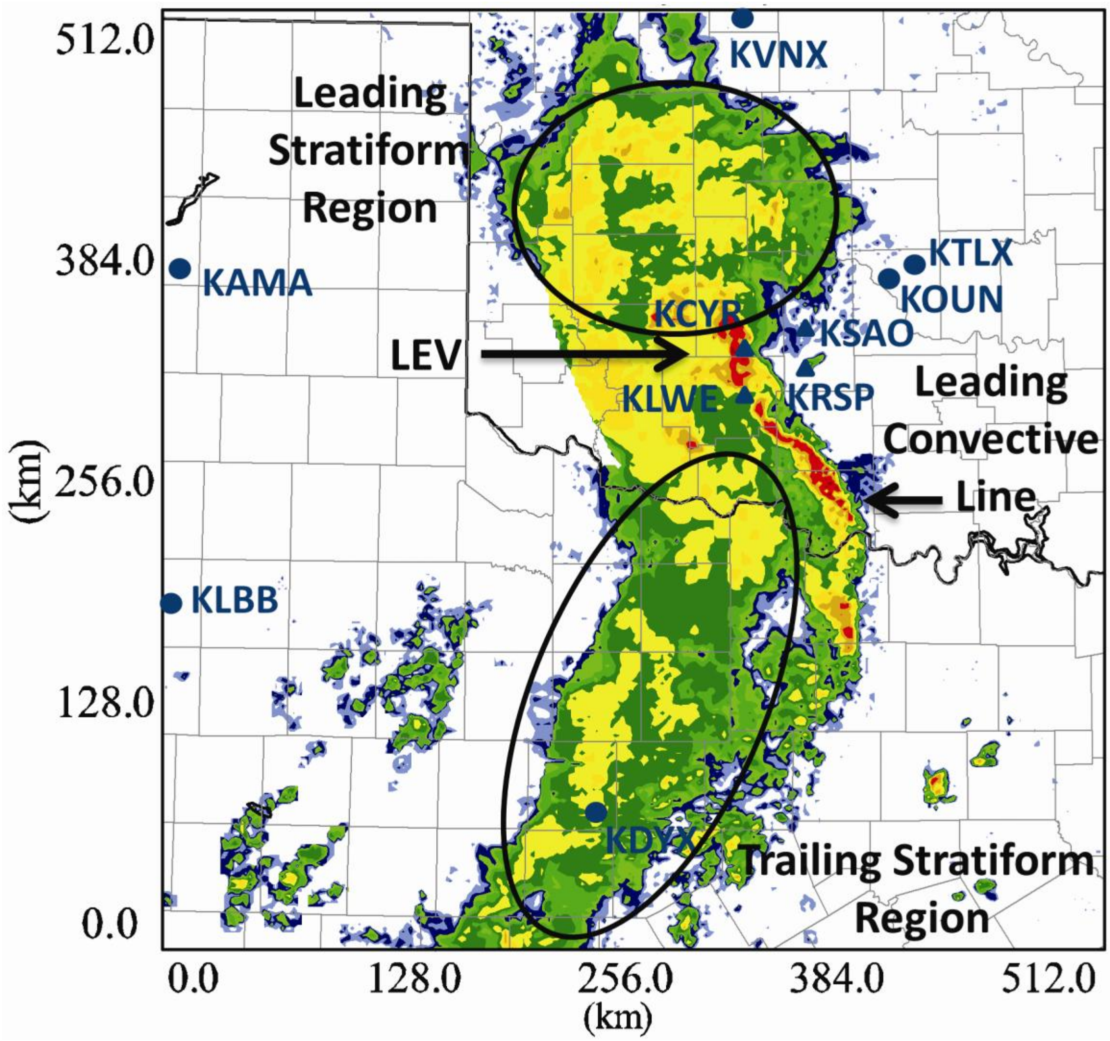

Fig. 2. Radar reflectivity (dBZ) observation mosaic from KAMA, KDYX, KFWS, KLBB, KTLX, and KVNX at 0200 UTC approximately 2km AGL covering the full experiment domain. Note the locations of the leading convective line, LEV, leading stratiform region, and trailing stratiform regions. The locations of all radars used in this study are also included.

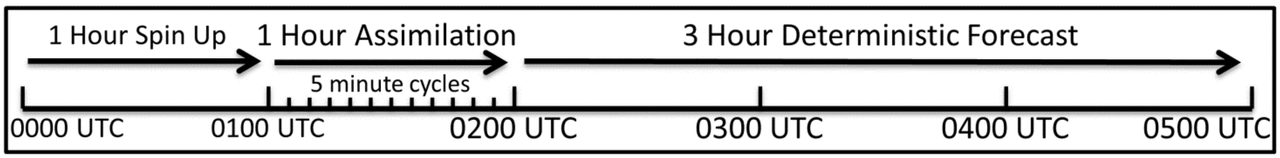

Fig. 3. Diagram of initial spin-up forecast, EnKF data assimilation cycles, and subsequent forecast for the experiments.

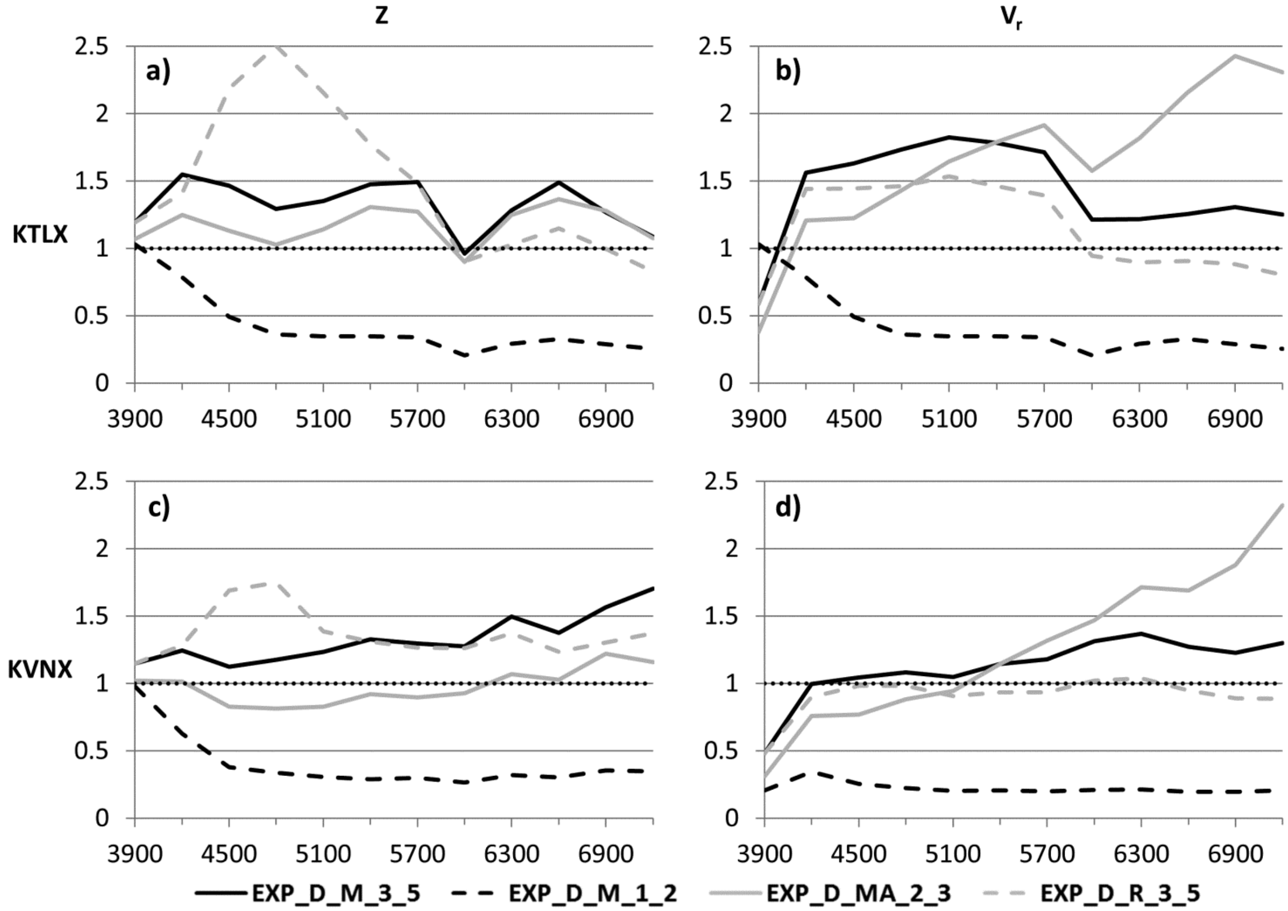

Fig. 4. Consistency ratios during the assimilation period (0105 UTC – 0200 UTC) of experiments EXP_D_M_3_5, EXP_D_M_1_2, EXP_D_MA_2_3, and EXP_D_R _3_5 for KTLX (a) Z and (b) Vr and KVNX (c) Z and (d) Vr data. The time is in seconds starting at 0000 UTC. The optimal value of 1 is indicated by the black dotted line.

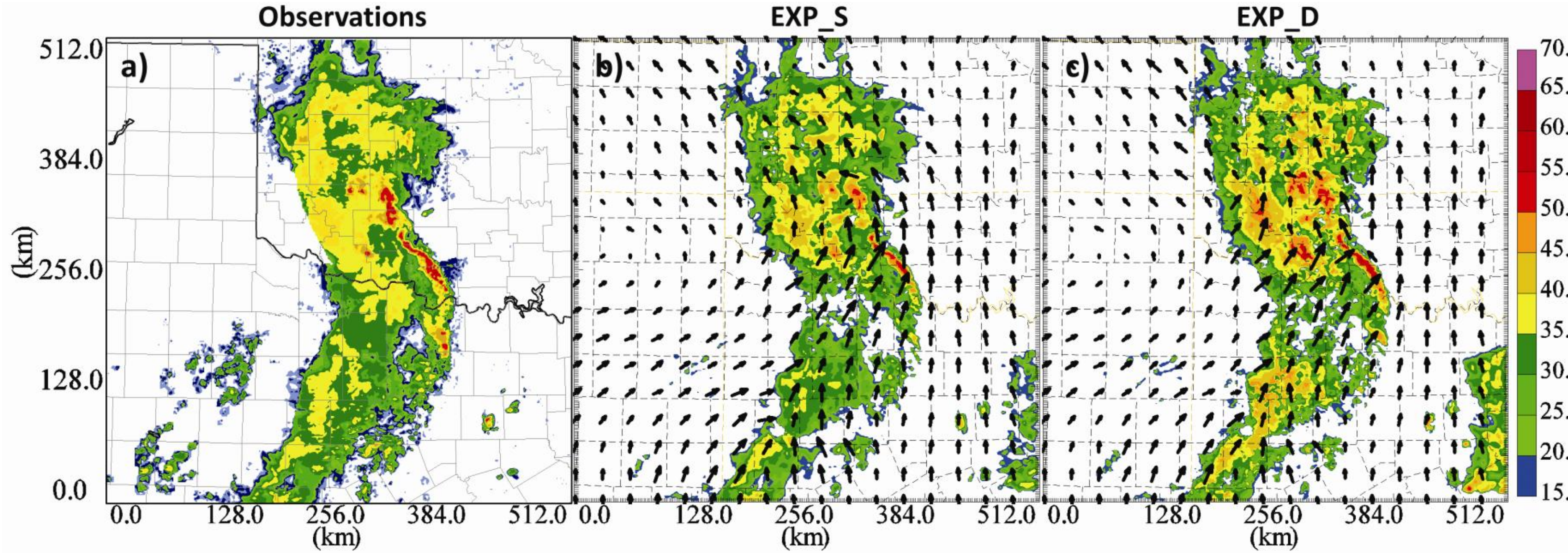

Fig. 5. (a) Reflectivity (dBZ) observation mosaic (a) from KAMA, KDYX, KFWS, KLBB, KTLX, and KVNX approximately 2 km AGL and analyzed reflectivity and horizontal wind vectors (m s^{-1}) at 0200 UTC plotted at grid level 10 (about 2 km AGL) for (b) EXP_S and (c) EXP_D. The horizontal wind vectors are plotted every 15 grid points (30 km).

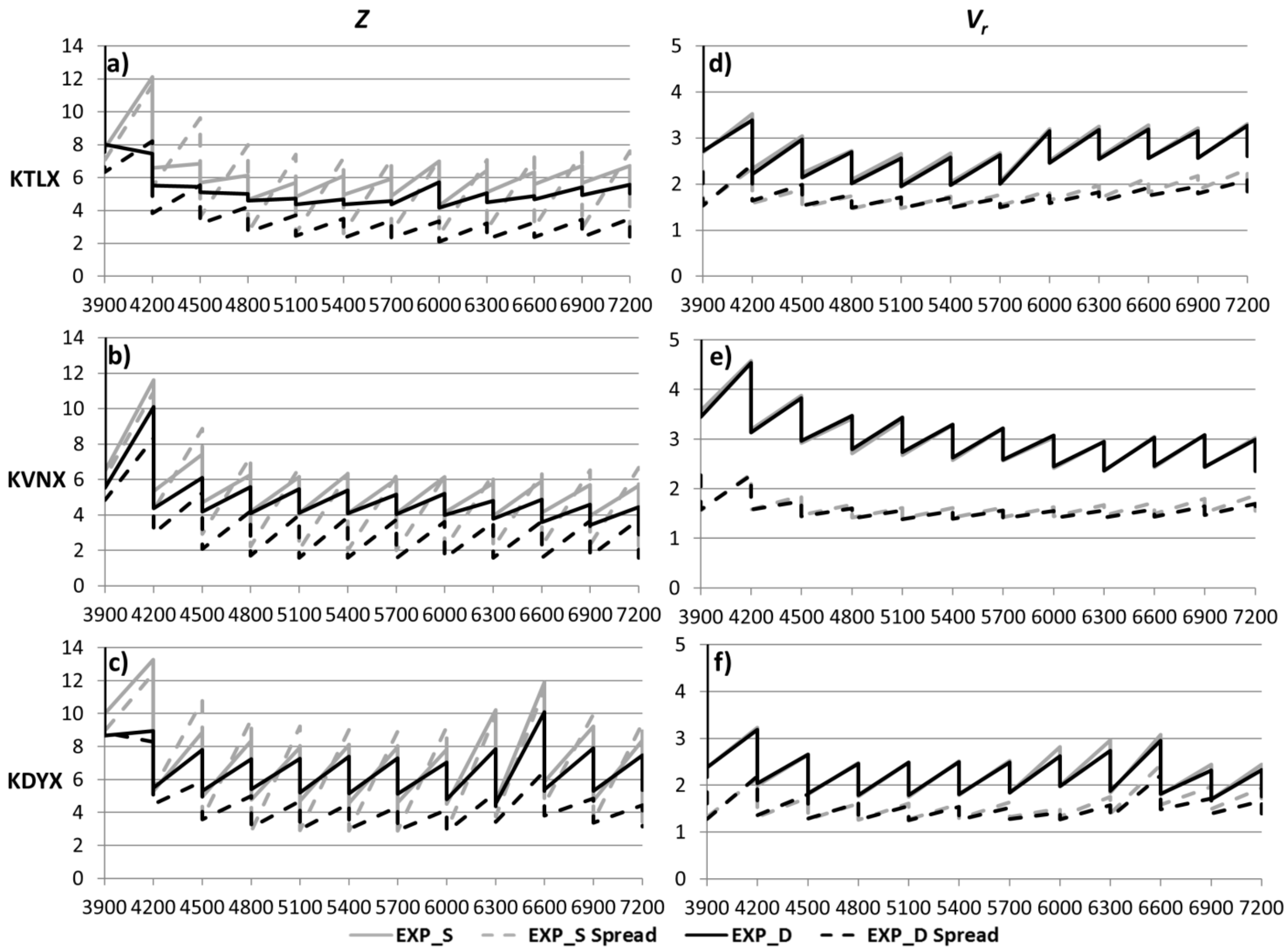

Fig. 6. Average root-mean-square innovation and ensemble spread during the assimilation period for EXP_S and EXP_D for reflectivity (dBZ) calculated against (a) KTLX, (b) KVNX, and (c) KDYX observations as well as (d-f) radial velocity (ms^{-1}). Time of assimilation is given in seconds based on the start of the experiment at 0000 UTC (0105 UTC – 0200 UTC).

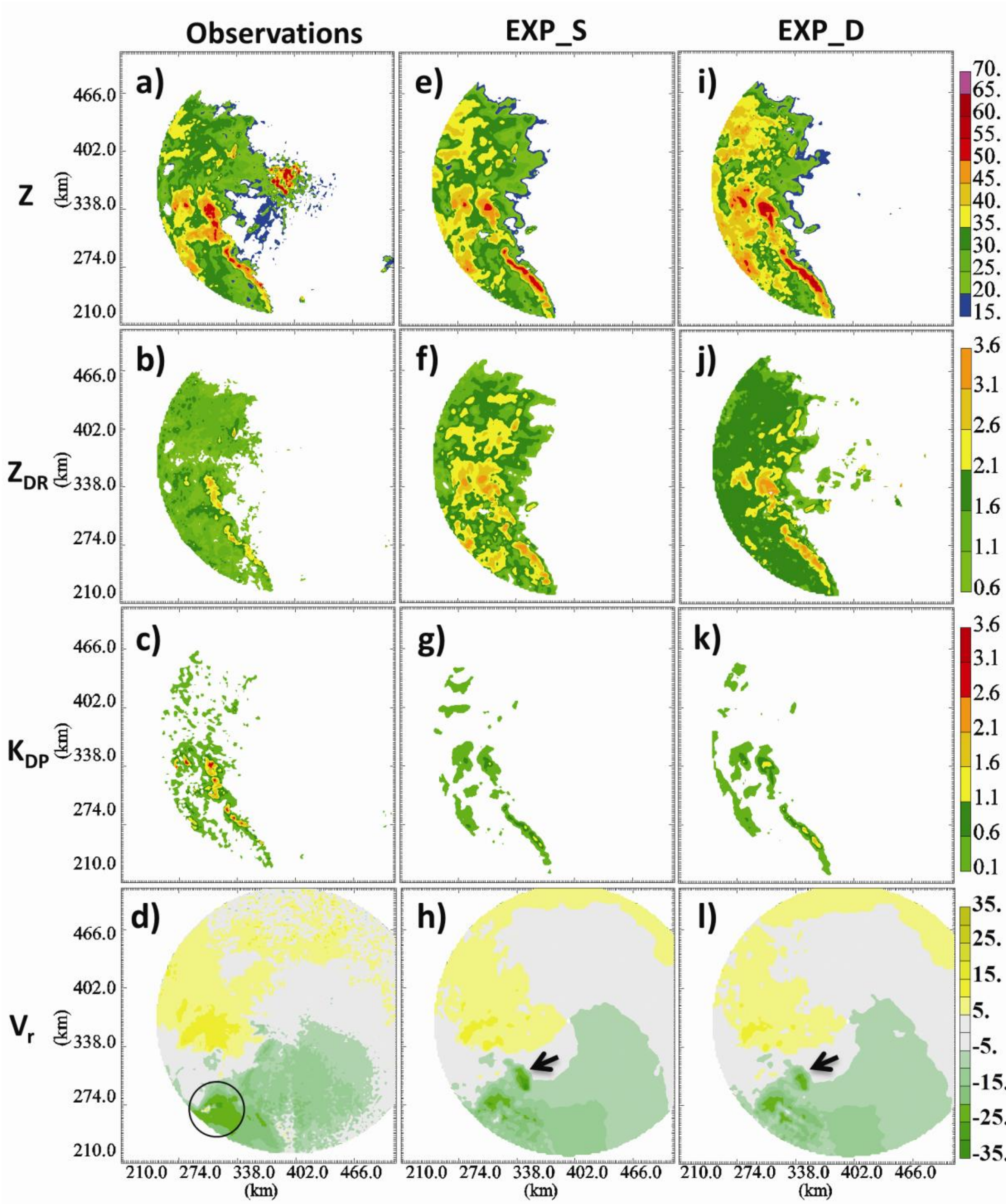

Fig. 7. (a) Reflectivity (dBZ), (b) differential reflectivity (dB), (c) specific differential phase (deg km^{-1}) , and (d) radial velocity (ms^{-1}) at a .5° tilt from KOUN as well as the ensemble mean final analysis at 0200 UTC for (e-h) EXP_S and (i-l) EXP_D.

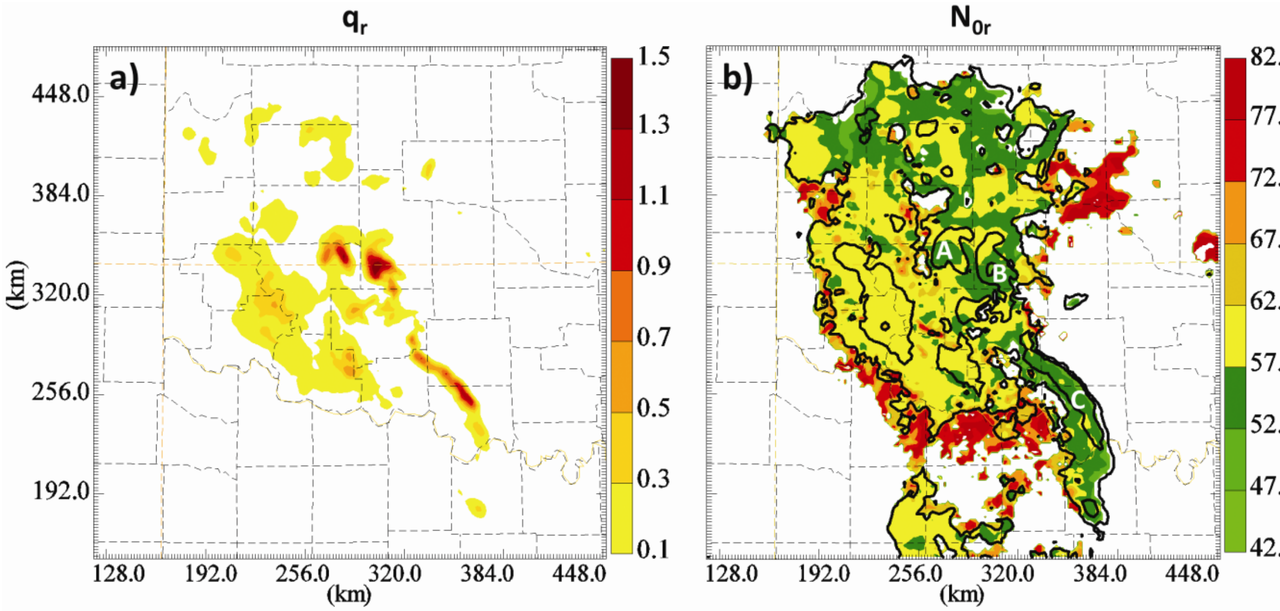

Fig. 8. Surface (a) rain water mixing ratio (g kg^{-1}) and (b) intercept parameter values (m^{-3} mm^{-1}, $10\log_{10}$ scale) from the EXP_D final ensemble mean analysis. Reflectivity contours at 20 dBZ intervals are overlaid on (b). The fixed intercept parameter value in EXP_S corresponds to 59 on the $10\log_{10}$ scale.

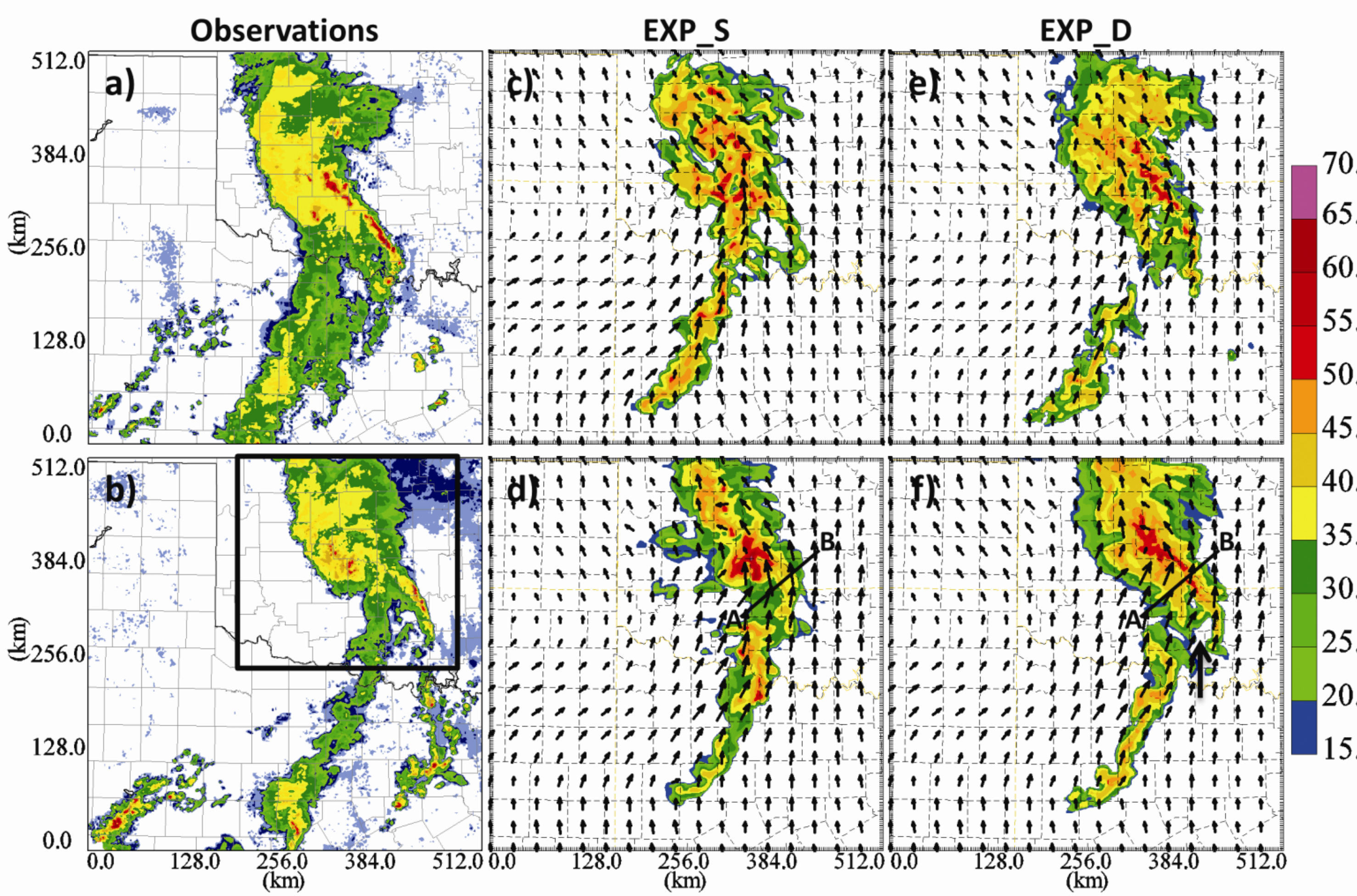

Fig. 9. Reflectivity (dBZ) observation mosaic from KAMA, KDYX, KFWS, KLBB, KTLX, and KVNX approximately 2 km AGL at (a) 0230 UTC and (b) 0400 UTC as well as (c) 30 minute and (d) 2 hour forecast reflectivity and horizontal wind field (m s^{-1}) at grid level 10 (about 2 km AGL) for EXP_S and (e, f) EXP_D. The horizontal wind vectors are plotted every 15 grid points (30 km).

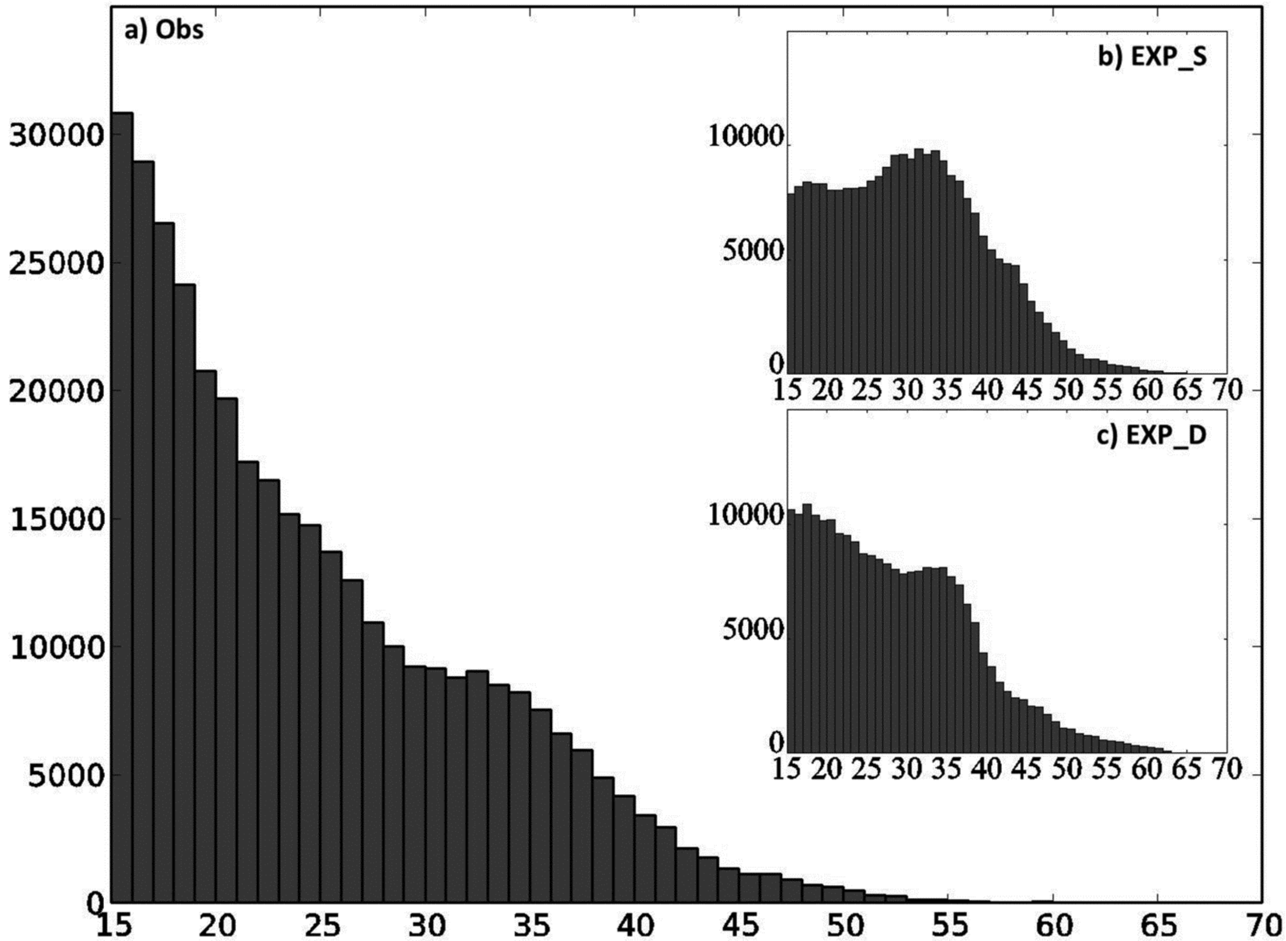

Fig. 10. Reflectivity frequency histograms plotted for 1 dBZ bins for (a) the KAMA, KDYX, KFWS, KLBB, KTLX, and KVNX radar reflectivity observation mosaic (one the same model grid) and for 2 hour forecast reflectivity from (b) EXP_S and (c) EXP_D.

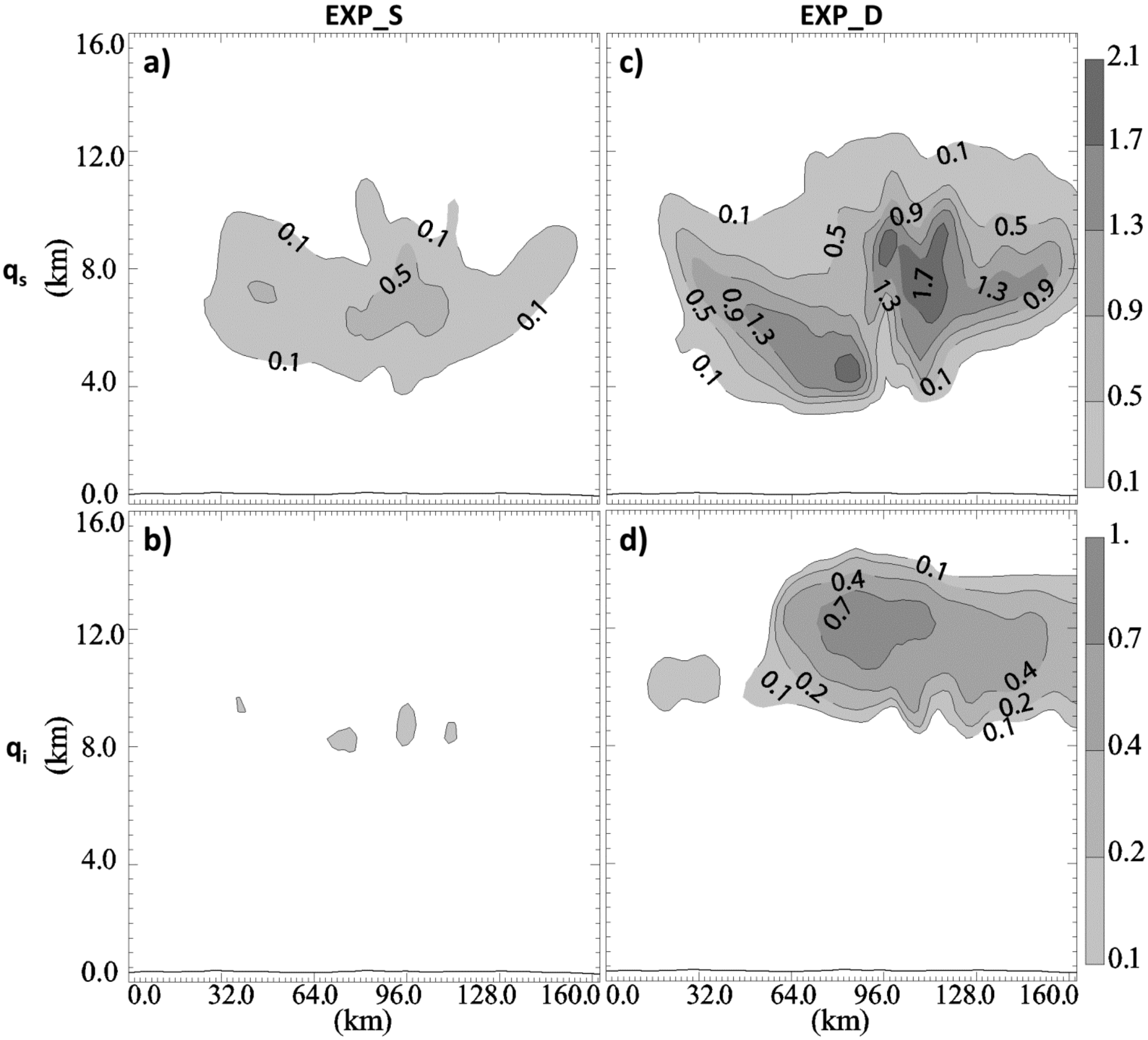

Fig. 11. Vertical cross sections of (a) snow mixing ratio (g kg^{-1}) and (b) cloud ice mixing ratio (g kg^{-1}) for EXP_S and (c-d) EXP_D. The locations of the cross sections are noted in Fig. 9d for EXP_S and Fig. 9f for EXP_D and extend from point A (left) to point B (right).

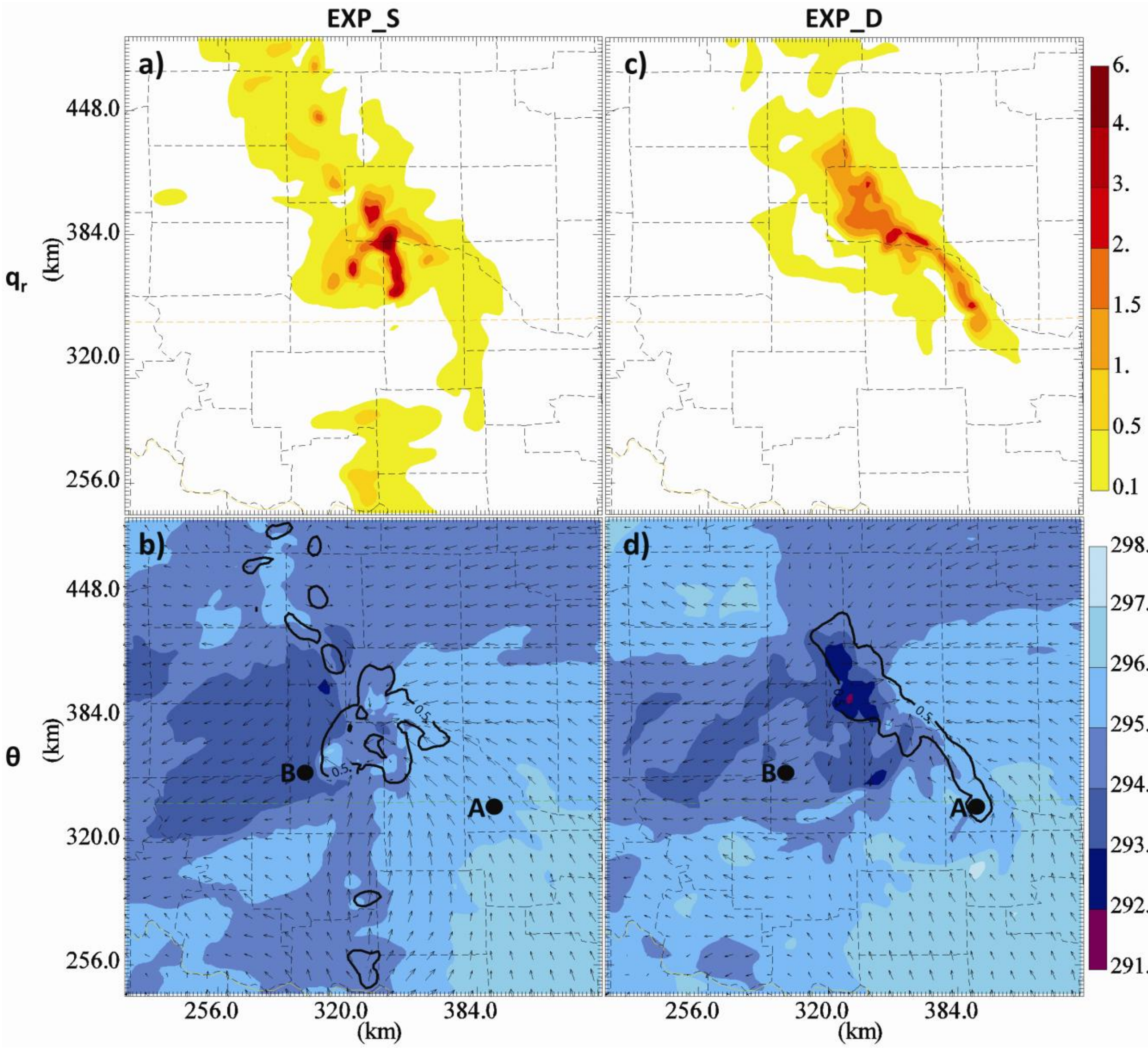

Fig. 12. Two hour forecast surface (a) rain water mixing ratio (g kg^{-1}) and (b) potential temperature (K) and horizontal wind field (ms^{-1}) for EXP_S and (c-d) EXP_D. The 0.5 g kg^{-1} rain water mixing ratio contour is overlaid on the potential temperature plots. Horizontal wind vectors are plotted every 5 grid points (10 km).

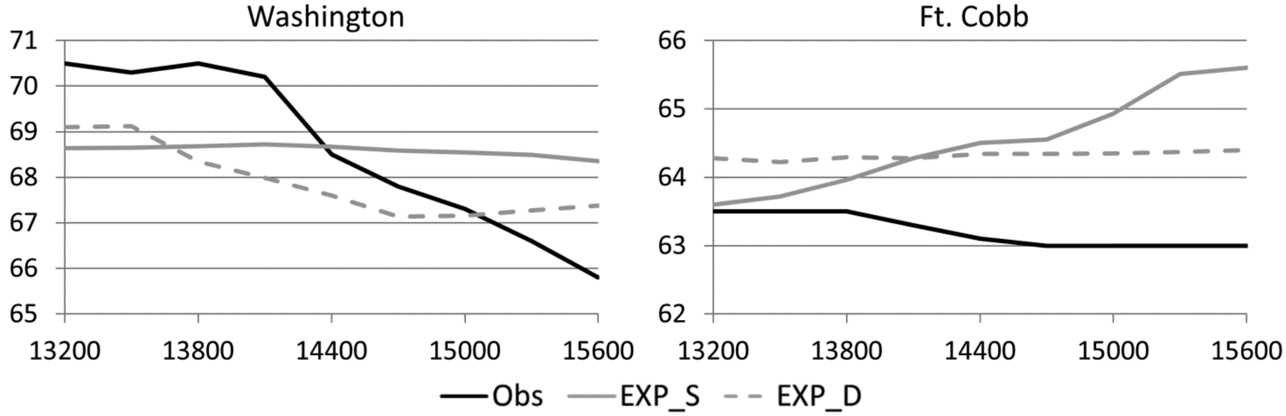

Fig. 13. Observed as well as interpolated surface temperature (°F) time series plots from EXP_S and EXP_D (UTC) at the location of Oklahoma Mesonet stations (a) Washington and (B) Ft. Cobb. The station locations are indicated by an ‘A’ for Washington and ‘B’ for Ft. Cobb in Fig. 11c and d.

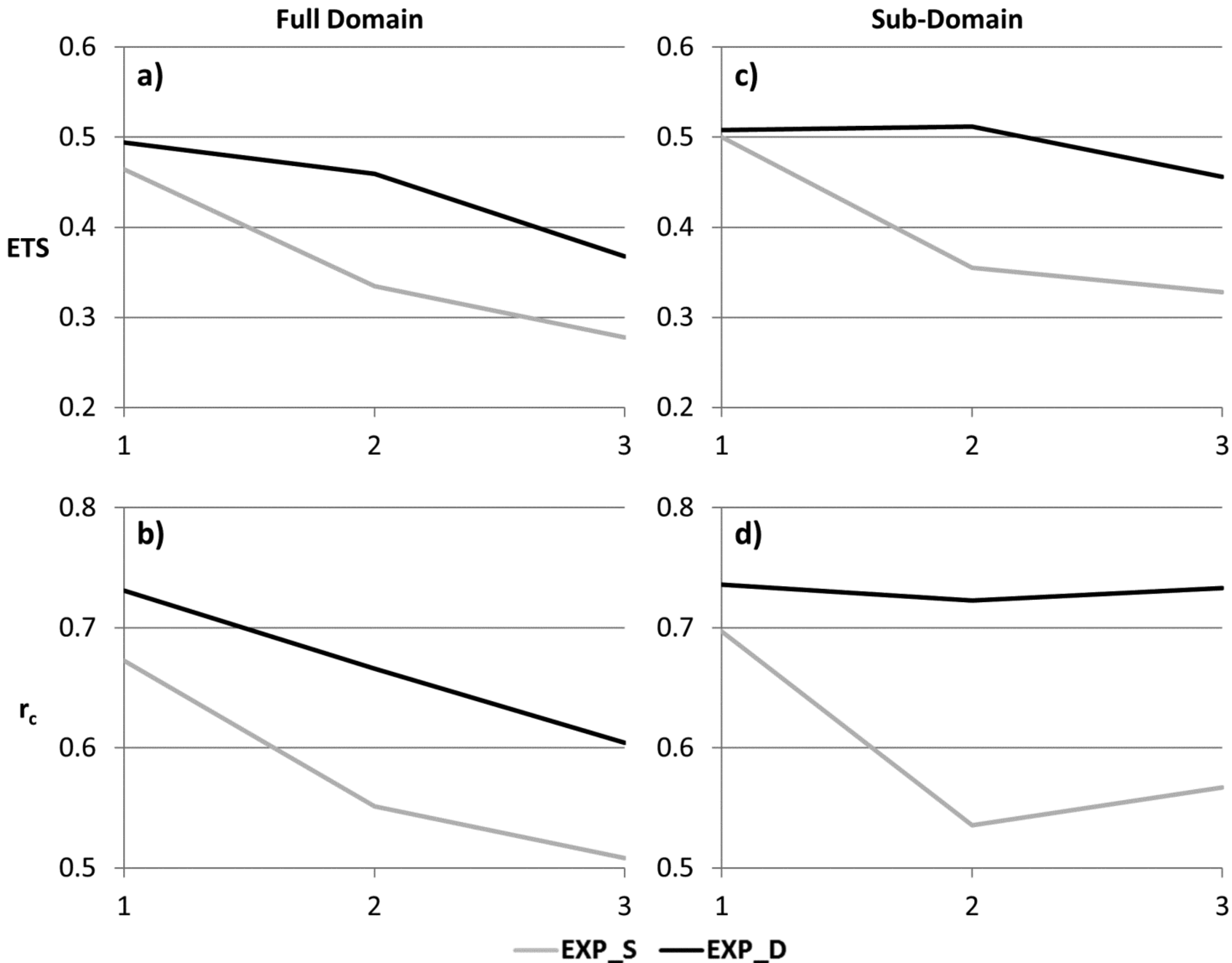

Fig. 14. (a) Forecast reflectivity ETS and (b) RCC scores for EXP_S and EXP_D at forecast hours 1, 2, and 3 for the entire experiment domain as well as over the (c-d) sub-domain defined in Fig. 9b.

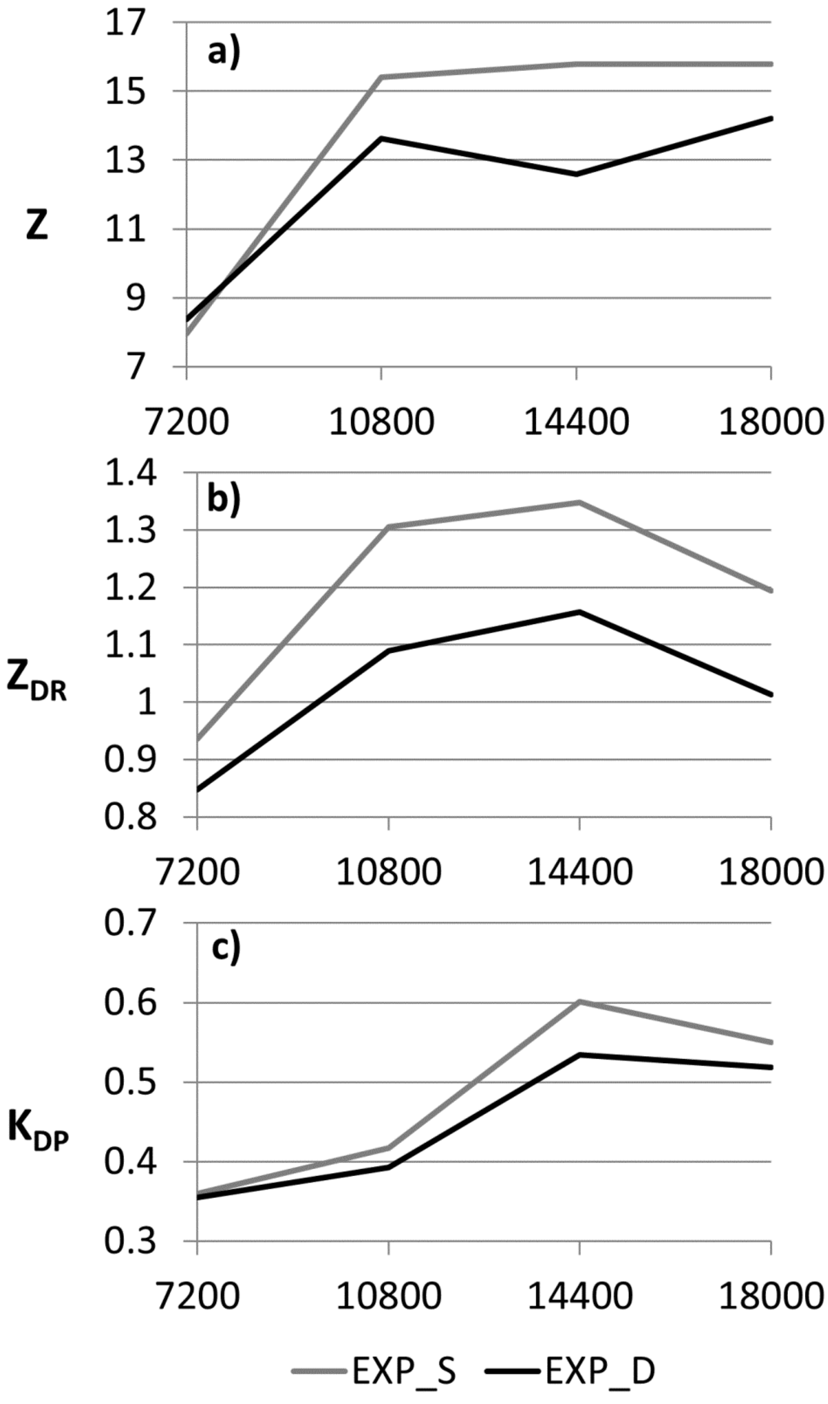

Fig. 15. The RMSDs between simulated polarimetric variables of EXP_S and EXP_D and KOUN observations at a 0.5° tilt for (a) reflectivity of horizontal polarization (dBZ), (b) differential reflectivity (dB), and (c) specific differential phase (deg km^{-1}) throughout the forecast period.